Geodynamic Importance of the Strike-Slip Faults at the Eastern Part of the Anatolian *Scholle*: Inferences from the Uplift and Slip Rate of the Malatya Fault (Malatya-Ovacık Fault Zone, Eastern Turkey)

Taylan Sançar, Cengiz Zabcı, Naki Akçar, Volkan Karabacak, Serdar Yeşilyurt, Müge Yazıcı, H. Serdar Akyüz, Ayten Öztüfekçi Önal, Susan Ivy-Ochs, Marcus Christl, Christof Vockenhuber

PII: S1367-9120(19)30443-2
DOI: https://doi.org/10.1016/j.jseaes.2019.104091
Reference: JAES 104091

To appear in: *Journal of Asian Earth Sciences*

Received Date: 8 April 2019
Revised Date: 10 September 2019
Accepted Date: 18 October 2019

Please cite this article as: Sançar, T., Zabcı, C., Akçar, N., Karabacak, V., Yeşilyurt, S., Yazıcı, M., Serdar Akyüz, H., Öztüfekçi Önal, A., Ivy-Ochs, S., Christl, M., Vockenhuber, C., Geodynamic Importance of the Strike-Slip Faults at the Eastern Part of the Anatolian *Scholle*: Inferences from the Uplift and Slip Rate of the Malatya Fault (Malatya-Ovacık Fault Zone, Eastern Turkey), *Journal of Asian Earth Sciences* (2019), doi: https://doi.org/10.1016/j.jseaes.2019.104091

Geodynamic Importance of the Strike-Slip Faults at the Eastern Part of the Anatolian *Scholle*: Inferences from the Uplift and Slip Rate of the Malatya Fault (Malatya-Ovacık Fault Zone, Eastern Turkey)

Taylan Sançar[1,2*], Cengiz Zabcı[3], Naki Akçar[4], Volkan Karabacak[5], Serdar Yeşilyurt[4] Müge Yazıcı[3], H. Serdar Akyüz[3], Ayten Öztüfekçi Önal[2], Susan Ivy-Ochs[6] Marcus Christl[6], Christof Vockenhuber[6]

[1]Munzur Üniversitesi, Edebiyat Fakültesi, Coğrafya Bölümü, 62000, Tunceli, Turkey.

[2]Rare Earth Elements Application and Research Center, Munzur University, 62000, Tunceli, Turkey.

[3]Istanbul Teknik Üniversitesi, Maden Fakültesi, Jeoloji Mühendisliği Bölümü, 34469 Istanbul, Turkey.

[4]Institute of Geological Sciences, University of Bern, Baltzerstrasse 1+3, CH-3012 Bern, Switzerland.

[5]Eskişehir Osmangazi Üniversitesi, Mühendislik Mimarlık Fakültesi, Jeoloji Mühendisliği Bölümü, Eskişehir, Turkey.

[6]Laboratory of Ion Beam Physics, ETH Zurich, CH-8093, Zürich, Switzerland.

*Corresponding author e-mail: tsancar@munzur.edu.tr

ABSTRACT

Controversy remains over when present-day configuration of the Anatolia boundary faults came into existence, and the issue of what are the driving forces of the Anatolian westward

motion. The NW-striking dextral and NE-striking sinistral second-order strike-slip faults at the eastern part of the Anatolian *Scholle* play a crucial role within these long-lasting discussions, and the NE-striking sinistral Malatya–Ovacık Fault Zone (MOFZ) is particularly important in this ongoing debate. Although the MOFZ is defined as one of the intra-plate structures, it has been proposed that it was an inter-plate fault between the Anatolia and Arabian plates from the latest Miocene to mid-Pliocene and that it has been inactive during the last ca. 3.5 Ma. This study provides results from the first morphochronology-based uplift and slip rate estimates on the Malatya Fault within the southern section of the MOFZ. The cosmogenic isochron burial and cosmogenic depth burial of ages from the sinistrally offset Tohma River remnant terraces enabled us to calculate 1.0 ± 0.01 and 1.12 ± 0.01 mm/yr minimum and maximum horizontal slip rates, respectively, for the last 1.4 ± 0.1 Ma. Furthermore, we conclude that the 96 ± 11 m/Ma mean uplift has been driven by the Malatya Fault. Integrated interpretation of the findings of this study and available data on both the MOFZ and other strike-slip faults at the eastern part of the Anatolian *Scholle* support the hypothesis that they are plate-boundary related active deformation belts that originated from paleotectonic structures during the tectonic escape of the Anatolian *Scholle*.

Keywords: Malatya Fault, Slip-Uplift Rate, Intraplate Deformation, Turkey

1. Introduction

The importance of the westward motion of the Anatolian *Scholle* (lump, clod of earth or flake in German, after Dewey and Şengör, 1979) within the geodynamic models of the eastern

Mediterranean region has long been the focus of many studies (e.g. Dewey and Şengör, 1979; Faccenna et al., 2013; Faccenna et al., 2006; Le Pichon, 1982; Le Pichon and Kreemer, 2010; McKenzie, 1972; McKenzie, 1978; Nyst and Thatcher, 2004; Şengör et al., 1985). The ongoing debates about the westward motion of the Anatolian *Scholle* can be treated under the following two headings: (a) *What are the driving forces behind the westward motion?* (b) *When did the present-day configuration of boundary faults of the Anatolian Scholle form*? The predictions and evaluations attributed to the internal deformation of the Anatolian *Scholle* have complementary and supportive roles in the models that deal with these questions, and therefore, it is necessary to increase knowledge thereof. However, fewer studies have focused on the internal deformation of the Anatolian *Scholle* compared to its boundary faults, the North (NAFZ) and East Anatolian Fault Zones (EAFZ) (Fig. 1a).

The ongoing northward convergence of the Arabian and African plates with respect to Eurasia give rise to the westward motion of the Anatolian *Scholle,* during which the NAFZ and EAFZ accommodate the main deformation (Le Pichon and Kreemer, 2010; Özeren and Holt, 2010; Şengör et al., 1985). Although earlier geologic studies proposed that the eastern part of the Anatolian *Scholle,* where internal deformation is characterized by a number of second-order NW- and NE- oriented strike-slip faults (Şengör, 1979; Şengör et al., 1985), accommodated an important amount of deformation that resulted from the convergence between the Arabian and Eurasian plates (Fig. 1a; Bozkurt, 2001; Kaymakcı et al., 2010; Koçyiğit and Beyhan, 1998; Rolland et al., 2012; Şengör et al., 1985), the initial geodetic studies were suggestive of minimal internal deformation (McClusky et al., 2000; Reilinger et al., 2006). Further studies have propounded that the evidence showing the activity of the second-order strike-slip faults in the eastern part of the Anatolian *Scholle* is not sufficient (Westaway, 1999;

Westaway and Arger, 2001; Westaway et al., 2008). However, recent evidences suggest that the westward motion has led to the accumulation of deformation within the eastern part of the Anatolian *Scholle* (Aktuğ et al., 2013a; Aktuğ et al., 2013b; Higgins et al., 2015; Özener et al., 2010; Sançar et al., 2018, 2019; Sarıkaya et al., 2015; Yazıcı et al., 2018a, b; Yıldırım, 2014; Yıldırım et al., 2016).

In this study, we focused on one of the most discussed, probably the most important, second-order strike-slip fault, the Malatya–Ovacık Fault Zone (MOFZ) (Fig. 1). There are two conflicting viewpoints currently being adopted in research into the MOFZ, namely, (a) that the MOFZ was the former southwest boundary of the Anatolian *Scholle* and has not been active since the mid-Pliocene (Westaway and Arger, 2001; Westaway et al., 2008) and (b) that the MOFZ is an actively deforming intra-plate structure (Kaymakçı et al., 2006; Koçyiğit and Beyhan, 1998; Şengör et al., 1985). Here, we used cosmogenic isochron burial and cosmogenic depth profile dating techniques to reconstruct the chronology of the sinistrally offset Tohma River terraces. The reconstructed chronology enabled us to calculate mid-Pleistocene slip and uplift rates of the southern part of the MOFZ, the Malatya Fault (Figs. 1a and 2). The results of this study contradict the claim that the MOFZ is not an active deformation belt (Westaway and Arger, 2001; Westaway et al., 2008), futhermore support the idea that the MOFZ is an active stucture (Kaymakçı et al., 2006) and have allowed us to discuss the causes of the widespread intra-plate deformation of the Anatolian *Scholle*.

2. Background

2.1. Active Tectonics of the Anatolian *Scholle*

The southern branch of the Neotethys Ocean closed entirely during the continent-continent collision between the northward-moving Arabian plate and Eurasian plate along the Bitlis-Zagros Suture Zone ca. 13 Ma ago that marked the beginning of the neotectonic period of Turkey (Şengör, 1980; Şengör et al., 1985; Şengör and Yılmaz, 1981). In addition to the effect of the Bitlis-Zagros subduction-collision, the Hellenic subduction and rollback are the primary mechanisms responsible for the complex tectonic settings in the eastern Mediterranean region (Le Pichon and Kreemer, 2010; Reilinger et al., 2006; Şengör et al., 1985). Paleomagnetic studies (Gürsoy et al., 1997; Gürsoy et al., 2011; Piper et al., 2010) revealed that these ongoing mechanisms give rise to anticlockwise rotation of eastern part of the Anatolian Block. Moreover, Global Positioning System (GPS) vectors point out the westward circular counterclockwise motion of the Anatolian *Scholle* with increasing rotational velocity from east to west with respect to Eurasia (Le Pichon and Kreemer, 2010). Different ideas have been proposed to explain the reason behind the westward motion (Chorowicz et al., 1999; Faccenna et al., 2013; Le Pichon and Kreemer, 2010; McKenzie, 1972; Özeren and Holt, 2010; Reilinger et al., 2006; Şengör et al., 1985); however, it has been conclusively shown that the NAFZ and EAFZ accommodate the main deformation of the Anatolian westward motion (Le Pichon and Kreemer, 2010; Reilinger et al., 2006; Şengör, 1980; Şengör et al., 1985, 2005).

The NW-striking dextral and NE-striking sinistral strike-slip faults represent the major deformational structures of the eastern part of the Anatolian *Scholle* (Fig. 1a). Their past tectonic role and modern activity have been one of the main axes of models that aim to explain not only their origin but also their relationship with the geodynamic conditions of the eastern Mediterranean region (Higgins et al., 2015; Kaymakçı et al., 2006; Koçyiğit and Beyhan,

1998; Şengör, 1979; Şengör et al., 1985; Westaway and Arger, 2001; Westaway et al., 2008). A pioneering hypothesis asserted that the simultaneous activity of the NAFZ and EAFZ caused the formation of the NW-striking dextral and NE-striking sinistral strike-slip faults (Şengör, 1979; Şengör et al., 1985). The next hypothesis proposed that the modern boundary faults of the Anatolian *Scholle* formed after the mid-Pliocene and the activity of the NW-striking dextral and NE-striking sinistral strike-slip faults either ceased or became not obvious since then (Westaway and Arger, 2001; Westaway et al., 2008). A more recent idea cautions that the West Anatolian Extensional Province has had a greater influence on central Anatolia than previously thought (Higgins et al., 2015).

2.2. Second-Order Strike-Slip Faults at the Eastern Part of the Anatolian *Scholle*

Although the eastern part of the Anatolian *Scholle* is characterized by a number of second-order strike-slip faults, only the dextral Tuz Gölü Fault Zone, the sinistral Central Anatolian Fault Zone, and the MOFZ have been documented in terms of the tectonic evolution, slip rate, and earthquake recurrence time.

2.2.1. The Tuz Gölü Fault Zone (TGFZ)

The NW–SE striking dextral with a normal slip component Tuz Gölü Fault Zone (TGFZ) can be described as an intra-plate structure (Fig. 1b) (Çemen et al., 1999; Dirik and Göncüoglu, 1996; Özsayın et al., 2013; Uygun et al., 1982). The TGFZ delimits the eastern margin of the Tuz Gölü Basin (Şaroğlu et al., 1992) that started to form during the late Maastrichtian (Çemen et al., 1999; Görür et al., 1984; Uygun et al., 1982). Çemen et al. (1999) proposed that regional

east–west compression caused the formation of the dextral TGFZ during the late Eocene–Miocene. Özsayın et al. (2013) asserted that the compressional regime continued until the late Miocene (6.81 ± 0.24 Ma) and then the ongoing NE–SW extensional regime was initiated during the Pliocene. Results from a GPS-based block model showed that the right lateral slip rate of TGFZ is 4.7 ± 0.1 mm/yr and its normal slip is 1.2 ± 0.1 mm/yr (Aktuğ et al., 2013b). Meanwhile, results from a paleoseismological investigation on the TGFZ showed that its southeast segment produced two earthquakes during the last 10.500 years (Kürçer and Gökten, 2012). The southernmost segment of the TGFZ produced 110-m vertical offset in Quaternary (Öztürk et al., 2018).

2.2.2. The Central Anatolian Fault Zone (CAFZ)

Koçyiğit and Beyhan (1998) proposed that the 730-km-long Central Anatolian Fault Zone (CAFZ) (Fig. 1b) may have formed from the propagation of a paleotectonic structure, the Ecemiş corridor, to the NE and SW directions during the neotectonic period of Turkey and accommodated compressive strain resulting from the convergence between the Arabian, African, and Eurasian plates. Higgins et al. (2015) asserted that the CAFZ is the result of two independently reactivated paleotectonic structures, namely, a suture zone in the NW and the Ecemiş Corridor in the SE. The NE segments of the CAFZ, which developed within the Inner Tauride suture, are presented by a broad sinistral strike-slip fault zone, but normal displacement increases along the SW segments of the CAFZ after it bends to the south near the southern end of the Erkilet Fault (Higgins et al., 2015). A study on the northernmost segment of the CAFZ, the Tecer Fault, revealed that two earthquakes occurred in the last 10 ka and estimated 1 mm/yr slip rates (Akyüz et al., 2012). Different morphochronology-based studies along the southernmost

segment of the CAFZ, the Ecemiş Fault, calculated a 4.2 ± 1.9 mm/yr horizontal slip rate for the mid–late Pleistocene (Sarıkaya et al., 2015) and 1.1 ± 0.4 mm/yr for the last 60 ka (Higgins et al., 2015).

2.2.3. The Malatya-Ovacık Fault Zone (MOFZ)

The NE-oriented, 275-km-long sinistral strike-slip MOFZ consists of two segments. The N65–70 oriented, 110-km-long Ovacık Fault extends between the Erzincan Basin and the Eynir where it juxtaposes the 165-km-long NE–SW oriented Malatya Fault (Fig. 1b). Earliest studies described the MOFZ as a fault-related structure by considering the N–NE trending sharp topographic lineation at the western margin of the Malatya Basin (Arpat and Şaroğlu, 1975; Muehlberger and Gordon, 1987). However, later studies discussed the activity and geometry of the MOFZ and introduced different hypotheses regarding both the internal deformation of the Anatolian *Scholle* and geodynamic settings of the eastern Mediterranean region. The studies about the MOFZ can be divided into two groups.

According to the first group, the geometry and activity of the boundary strike-slip faults between the Anatolian, African, and Arabian plates during the latest Miocene to mid-Pliocene were significantly different from the present day. Westaway and Arger (1996) suggested that the boundary between the Anatolia and Arabia was delineated by the MOFZ until 3 Ma ago and its activity ceased when the EAFZ formed. This claim is modified in some of the later studies, e.g., ca. 3 Ma ago (Westaway and Arger, 2001), ca. 4 Ma ago (Westaway, 2003), ca. 3.73 ± 0.05 Ma ago (Westaway et al., 2006), ca. 3.5 Ma ago (Westaway et al., 2008), ca. 2.6 Ma ago (Hubert-Ferrari et al., 2009). Westaway et al. (2001) suggest that the MOFZ has been inactive since the middle Pliocene based on the absence of seismic activity described by Jackson and McKenzie (1984), recent faulting indicators, and necessary deformational structures around the junction of

the MOFZ and NAFZ. Westaway et al. (2008) proposed that there is no evidence to contradict the fact that the MOFZ has been inactive since the mid-Pliocene.

In contrast to the first group, Koçyiğit and Beyhan (1988) proposed that not only the MOFZ but also the other second-order strike-slip faults within the eastern part of the Anatolian *Scholle* accumulate part of the deformation during the westward extrusion of Anatolia and these are actively deforming intra-plate structures. Kaymakcı et al. (2006) identified strike-slip related morphotectonic structures that point out the short-term activity of the MOFZ and concluded that post-middle Miocene compression caused the reactivation of the early to late Miocene normal faults as sinistral strike-slip faults that formed the Malatya fault and some segments of the Ovacık fault. Kaymakcı et al. (2006), measured that the maximum deflection of Euphrates River, which controlled by Ovacık Fault, is 9.3 km and the cumulative deflections along the different part of the Ovacık Fault is not more than 20 km.

Furthermore, Kaymakcı et al. (2006) proposed the following three deformation phases for the Malatya Basin: (1) the NW–SE extension in the early to middle Miocene, (2) the WNW–ESE compression, which caused transcurrent tectonics in the late Miocene to middle Pliocene, and (3) NNE–SSW compression during the late Miocene to present. Recent GPS measurements have revealed a considerable amount of strain accumulation along the MOFZ (Özener et al., 2010). With GPS-based elastic block models, horizontal slip rates of 1.2 ± 0.3 mm/yr and 1.8 ± 0.1 mm/yr were calculated for the Ovacık Fault, whereas rates of 1.6 ± 0.3 mm/yr and 1.2 ± 0.1 mm/yr were obtained for the Malatya Fault (Aktuğ et al., 2013a,b). The more recent paleoseismological studies on the Ovacık and Malatya faults have revealed that four palaeoevents occurred during the last 10 ka and estimates of 1600 ± 515 years (Yazıcı et al., 2018a) and 2275 ± 605 years (Sançar et al., 2019) were obtained for the average earthquake

recurrence interval, respectively. Duman et al. (2017) divide Malatya Fault into three segments and Sançar et al. (2019) defined five segments along the 165-km-long Malatya Fault based on its surface geometry (Fig. 2). The FS-1, which forms the northernmost part of the Malatya Fault, is distinguished from the FS-2 by an eastward arc-shaped geometry. The Kızık Basin, which is one of the prominent geometric discontinuities, separates the FS-2 and FS-3. To the south of Akçadağ, the Malatya Fault bifurcates into two parallel branches, which are named as the FS-4 and FS-5 (Fig. 2). All these segments show clear morphotectonic structures related to both long- and short-term fault activity (Sançar et al., 2019). Furthermore, more recent small to moderate sized earthquakes (up to Mw=4.5) in March 2019 on the western block of the Malatya Fault (near Kızık Basin) are another indicators of the ongoing fault activity (URL, 2019).

3. Methods

3.1. Mapping

We improved the previous geology map in the vicinity of the Tohma River basin (Bedi and Yusufoğlu, 2018; Sümengen, 2016) using detailed mapping data from the field and digital aerial photographs at ca. 0.4-m ground pixel resolutions. The spatial distribution of the key geomorphic (terrace remnants) and morphotectonic structures around the Tohma River were determined by a stereoscopic digital aerial photo-based Digital Elevation Model, which was produced using 25-cm interval elevation contours.

3.2. Offset Determination and Terrace Elevation

The climate and uplift are the driving mechanisms that caused the formation of the Quaternary staircase terraces, and the uplift ratios constitute important parameters related to both the generation and preservation of terraces (Bridgland, 2000; Maddy et al., 2001; Pan et al., 2009; Pazzaglia, 2013; Wang et al., 2015). Therefore, determination of the ages and positions of the remnant fluvial terraces with respect to a reference level has become a key tool for the quantification of incision rate-based uplift (Çiner et al., 2015; Peters and van Balen, 2007; Ruszkiczay-Rüdiger et al., 2016). The base level of the modern river, which is graded to sea level (Erlanger et al., 2012), presents the reference elevation for the calculation of river incision. However, if the long-profile of the river is considerably away from the sea-level, the incision does not reflect the sea-level fluctuations (Merritts Dorothy et al., 2012). We, therefore, assumed that the calculated incision rate from the E–W flowing Tohma River's staircase terraces does not reflect the sea-level changes and is equal to rock uplift (Fig. 3). The elevation differences between the Tohma River terraces and modern river were considered as the first inputs for the uplift rate calculations (Fig. 3).

We produced two slip scenarios to estimate the possible slip rate range. The spatial distribution of the remnant terraces and modern channel at both sides of the fault were used to produce offset scenarios that were the first inputs for calculation of the slip rate.

3.3. Cosmogenic Nuclide Dating and Sample Preparation

In order to interpret the chronology of the Tohma terraces, which represented the second type of input for both slip and uplift rate calculations, the isochron burial (with cosmogenic ^{10}Be and

^{26}Al) and depth profile (with cosmogenic ^{36}Cl) dating methods were performed on the collected samples. Samples from the Tohma terraces were prepared for the analysis of cosmogenic ^{10}Be, ^{26}Al and ^{36}Cl at the surface exposure dating laboratory of Bern University.

3.3.1. Isochron Burial Dating

Isochron burial dating with ^{26}Al and ^{10}Be nuclides has been used as an important tool for dating Plio–Pleistocene glaciations (Balco and Rovey, 2008; Balco et al., 2013), investigating sedimentary fills (Balco et al., 2013), calculating long-term river incision and uplift rates (Bender et al., 2016; Çiner et al., 2015; Darling et al., 2012; Erlanger et al., 2012; Zhao et al., 2016), and studying glacio-fluvial deposits (Akçar et al., 2017). The isochron burial dating technique is based on the analysis of cosmogenic ^{26}Al and ^{10}Be in quartz in deposits (sand or >50 clasts) (Balco and Rovey, 2008). Because ^{26}Al and ^{10}Be have different half-lives, these nuclides decay at different rates (Balco and Rovey, 2008). By using the ^{26}Al/^{10}Be ratio difference between the surface production at the time of burial and that measured in buried sediment, one can obtain a calibration of the burial time (Granger, 2006). In order to reconstruct the isochron burial history, several samples from a single stratigraphic horizon, which indicate the same post-burial history, are required. However, the pre-burial exposure histories of the samples are most likely not the same, and therefore, the yielded inherited nuclide concentrations are different; this allows for the modeling of the ^{26}Al/^{10}Be ratio at the time of burial, which is known as the post-burial component (Balco and Rovey, 2008; Bender et al., 2016; Erlanger et al., 2012). Distinguishing the post-burial history of the deposits is the main advantage of isochron burial dating that makes this method independent from the post-burial accumulation and erosional modification approach (Balco and Rovey, 2008). Therefore, the method is appropriate for the ca. 2-m thin quartz-

bearing terrestrial deposits (Akçar et al., 2017; Balco and Rovey, 2008; Balco et al., 2013; Bender et al., 2016; Claude et al., 2019; Darling et al., 2012; Erlanger et al., 2012; Granger, 2006; Zhao et al., 2016).

3.3.2. Depth Burial Dating

The depth profile dating method was used to determine the chronology of fluvial terraces and cosmogenic nuclide inheritance (Anderson et al., 1996; Hancock et al., 1999; Repka et al., 1997). As the surface sample inheritance is large, collecting samples from the tops of the terrace deposits to downward positions allows for the separation of the inherited component of the total cosmogenic-nuclide from the in situ component (Anderson et al., 1996; Gosse and Phillips, 2001; Hancock et al., 1999; Repka et al., 1997). This method is based on the physical principles that govern the accumulation of cosmogenic nuclides, which predictably decrease exponentially with depth (Gosse and Phillips, 2001; Hancock et al., 1999).

3.4. Sample Preparation and Analysis for Isochron Burial Dating

We used the method of Akçar (2006), which is a modified version of Kohl and Nishiizumi (1992), in order to separate and purify quartz. Cosmogenic ^{26}Al and ^{10}Be were extracted according to the laboratory protocol of Akçar et al. (2012a) for accelerator mass spectrometer (AMS) measurements at ETH Zurich (Christl et al., 2013; Kubik and Christl, 2010). The 0.5 MV TANDY facility was used for both ^{26}Al and ^{10}Be analyses. Total Al and native ^{9}Be concentrations of the samples were determined by inductively coupled plasma optical emission spectrometry (ICP-OES) at the Department of Chemistry and Biochemistry of the University of

Bern. The applied weighted mean average ratio for $^{10}Be/^{9}Be$ was (2.51±0.13) × 10^{-15}. The CRONUS-Earth exposure age calculator, which uses the 07KNSTD standardization (http://hess.ess.washington.edu/math/ [v. 2.3] Balco et al., 2008, updated from v. 2.3, published by Balco in June 2016), was used to calculate the cosmogenic $^{26}Al/^{10}Be$ ratios. We applied 4.00 ± 0.32 atoms/gSiO_2/a (Borchers et al., 2016) as the production rate of cosmogenic ^{10}Be at the surface due to spallation at sea level–high latitude (SLHL). Although the surface production ratio of $^{26}Al/^{10}Be$ depends on the geographical position (Borchers et al., 2016), we opted to use 6.75 reference ratio (Balco and Rovey, 2008), which is generally used (Akçar et al., 2017; Balco and Rovey, 2008; Balco et al., 2013; Bender et al., 2016; Çiner et al., 2015; Erlanger et al., 2012; Zhao et al., 2016), to calculate the isochron burial ages. Altitude/latitude scaling of the surface production rate was calculated according to the time dependent Lal (1991)/Stone (2000) scheme (Lm). The density of quartz was taken as 2.65 gr/cm^3 for isochron burial dating, and half-lives of 1.39 Ma (Chmeleff et al., 2010; Korschinek et al., 2010) and 0.71 Ma (Nishiizumi, 2004; Norris et al., 1983) were used for ^{10}Be and ^{26}Al respectively. We assumed mean lives of 2.005 Ma for ^{10}Be and 1.02 Ma for ^{26}Al in the calculations.

3.5. Sample Preparation and Analysis for Depth Profile Dating

The samples that were used for cosmogenic ^{36}Cl analyses were prepared according to the procedure of Akçar et al. (2012b), which is based on Stone et al. (1996), by using isotope dilution (Desilets et al., 2006; Elmore et al., 1997; Ivy-Ochs et al., 2004). In order to determine the local ^{36}Cl production rate, major and trace element concentrations (from leached aliquots ca. 10 gr from each sample) and analyses of uranium (U), thorium (Th), boron (B), gadolinium (Gd), and samarium (Sm) were measured at Activation Laboratories, Ontario, Canada. Both total Cl

and ^{36}Cl concentrations were measured from one target with isotope dilution (Synal et al., 1997) at the ETH AMS facility by using a 6 MV TANDEM accelerator.

The $^{36}Cl/^{35}Cl$ sample ratio was normalized according to K382/4N, which is the ETH internal standard, with a value of $^{36}Cl/^{35}Cl = 17.36 \times 10^{-12}$ (normalized to the Nishiizumi standard in 2009). The stable $^{37}Cl/^{35}Cl$ ratio was normalized to the natural ratio $^{37}Cl/^{35}Cl = 31.98\%$ of the K382/4N standard and the machine blank.

We used a modified version of the Mathcad® code for ^{10}Be depth profile modeling provided by Hidy et al. (2010) in order to model the cosmogenic ^{36}Cl depth profile ages (after Claude et al. 2019). All production pathways of cosmogenic ^{36}Cl, such as high-energy neutrons, fast and negative muons, and thermal and epithermal neutrons were included (Alfimov and Ivy-Ochs, 2009; Liu et al., 1994; Phillips et al., 1996,2001; Schimmelpfennig et al., 2009; Stone et al., 1996,1998). We applied following values for the ^{36}Cl spallogenic production rates: 48.8 ± 3.5 atoms ^{36}Cl (g Ca)$^{-1}$ a^{-1} (Stone et al., 1996); 161 ± 9 atoms ^{36}Cl (g K)$^{-1}$ a^{-1} (Evans et al., 1997); 13 ± 2 atoms ^{36}Cl (g Ti)$^{-1}$ a^{-1} (Fink et al., 2000); and 1.9 ± 0.5 atoms ^{36}Cl (g Fe)$^{-1}$ a^{-1} (Stone, 2005). A value of 760 ± 150 neutrons (g air)$^{-1}$ a^{-1} was applied for the production of ^{36}Cl through neutron capture (Alfimov and Ivy-Ochs, 2009). For depth profile dating, the density of a calcareous pebble was taken as 2.4 gr/cm^3 and the half-life of 0.301 Ma for ^{36}Cl was used (Nica et al., 2012).

4. Results

4.1. Geology of the Tohma Site

The Tohma River drainage basin and its surroundings are characterized by four lithological units. The oldest unit in the study area, the Medik Formation (Tpm), crops out in the western part of the study area (Fig. 3). This unit consists of reddish brown, poorly sorted, semi-angular Jurassic-Cretaceous limestone and consolidated volcaniclastic pebbles, and its maximum thickness is ~1400 m (Hakyemez and Örçen, 1982). The age of this unit has been assigned to the Paleocene based on the stratigraphic relationship with the middle–upper Eocene Darende Formation (Ted) (Hakyemez and Örçen, 1982). The Darende Formation, which is made up of greenish-light gray conglomerate interbedded with sandstone, siltstone, limestone, marl alternations, and abundant amounts of evaporitic lenses, unconformably overlies the Medik Formation (Gürbüz and Gül, 2005; Sümengen, 2016). The limestone and marl of this formation contain middle-upper Eocene trace fossils (Bedi et al., 2009). The Beylerderesi Formation crops out in the eastern part of the study area and is composed mainly of strongly consolidated, poorly sorted limestone, and basalt fragments of the Medik Formation within a mud and sand matrix (Figs. 3 and 4a). It was described as alluvial fan deposits by Ercan (2011), and the Plio–Quaternary age was assigned in regard to the stratigraphic relationships with the surrounding units in the study area (Karaman et al., 1993). The Beylerderesi Formation unconformably overlies the Medik Formation except for in the southwestern part where the Malatya Fault delimits their boundary. We identified two levels of river terraces (T1 and T2) that are only preserved in a limited area. These terrace levels are present on both sides of the Tohma River Valley (Fig. 3). The abundant amount of microcrystalline quartz (chert) and granite pebbles within the terrace levels are the main lithological differences between the terrace levels and underlying units. The sedimentary structures, such as cross-lamination, within the terrace

deposits are indicative of the fluvial depositional environment (Fig. 4b). The swath topographic profiles (Fig. S1), which are perpendicular to the terraces on both sides of the river, reveal the staircase terrace formation and also indicate that the terrace elevation decreases from west to east (Figs. S2 and S3). Both terrace levels have been eroded by secondary fluvial activities (Fig. S1). Furthermore, the ongoing agricultural activity and construction of artificial channels has changed the original terrace level in the north (Fig. S4). Therefore, we preferred to sample the terrace system to the south, where terraces are well preserved (Fig. 3 and S4). The youngest unit is represented by the alluvium (Qal) that was deposited in the current channels (Fig. 3).

The FS-3, with a length of ca. 50 km, constitutes the longest segment of the Malatya Fault (Fig. 2). This segment is characterized by many morphologic structures that reflect the recent fault activity (Sançar et al., 2019). The clear fault-related structures to the north and south of the Tohma River, which flows nearly perpendicular to the FS-3, have been used to define the precise geometry of the Malatya Fault in the study area. At the locations north of the Tohma River (Fig. 3), the elongated depression within the Beylerderesi Formation represents the most pronounced structure (Fig. 5a). To the south of the Tohma River (Fig. 3), several sinistral displacement gullies within the Medik Formation represent the relatively short-term activity of the Malatya Fault (Fig. 5b).

4.2. Terrace Chronology

The T2 level was sampled at one locality for cosmogenic isochron-burial dating (THM-IS-T4, in Fig. 6), whereas the T1 level was sampled in three localities for cosmogenic isochron

burial (THM-IS-T2 at the aggradational terrace and THM-IS-PQ at the strath terrace in Fig. 6) and cosmogenic depth profile dating (THM-DP-T2 at the strath terrace in Fig. 6).

The swath profiles of P1 (see Fig. 6 for the location) show that the sampling site for the T2 terrace was located 106 m above the current Tohma River level that flows at 731 m above the sea level (Fig. 7a). The P2 profiles (see Fig. 6 for the location) show that T1 is separated from T2 and the modern channel by the T1–T2 riser and T1–Qal riser, respectively (Fig. 7b). The lower base of the T1 terrace is at 28 m, and its upper surface is at 34 m above the Tohma River (flows 724 m above sea level); its maximum thickness is 6 m (Fig. 7b). The THM-IS-T2 and THM-DP-T2 sampling sites, which were very close to each other, were located 28 m and 30 m above the modern Tohma River, respectively (Fig. 7b). The THM-IS-PQ locality was ca. 400 m east of the THM-IS-T2 locality and 29 m above the Tohma River (Figs. 6a and S3d).

The thickness of the T2 terrace deposits at the THM-IS-T4 locality is ca. 7 m, and these deposits contain spherical and well-rounded chert covered by ca. 1 m of fine-grained calcareous sandy sediments (Fig. 8). We collected seven chert clasts (8–15 cm in diameter) for isochron burial dating from 1 m below the terrace surface (sample location THM-IS-T4, shown in Fig. 6; Table 1). At the THM-IS-T2 locality, where we sampled for isochron burial dating, the ca. 2 m thick terrace deposits are composed of pebbly quartz deposits (Figs. 9a and b). Although T1 is mainly represented by gravels, a few sand bars that show the cross-bedding also have been preserved to the east of this terrace level. We collected 11 chert clasts (6–13 cm in diameter) for isochron burial dating from the surface from the natural outcrop of T1 (sample location THM-IS-T2, shown in Fig. 6; Table 1). Furthermore, we collected seven chert clasts (7–12 cm in diameter) at the THM-IS-PQ locality, where there is an ca. 70 cm thick strath terrace deposit (Fig. 9c), for isochron burial dating (sample location THM-IS-PQ, shown in Fig. 6; Table 1). In

comparison to the lower surface of T1, the upper surface is composed of loose pebbles, which we think are a sign of possible ongoing erosion. To avoid any post-depositional effects, we excavated a trench down to ~2 m from the lower surface of the T1 terrace (Fig. 9d). Five sediment samples (each ca. 1 kg) were taken every 25–30 cm down from the top of the trench for depth profile dating (sample location THM-DP-T2, shown in Fig. 6; Table 1).

Results of the cosmogenic ^{10}Be and ^{26}Al analyses are provided in Tables 2 and S1. Among the 25 clasts collected from the three sites, we obtained 13 at the end of leaching with appropriate weights and total Al concentrations, and these were selected for dissolving (Table S1). Measured ^{10}Be concentrations varied between (5.31 ± 0.39) × 10^4 and (91.64 ± 2.09) × 10^4 atoms/g, and measured ^{26}Al concentrations varied between (54.33 ± 3.81) ×10^4 and (229.46 ± 6.92) × 10^4 atoms/g (Table 2). The applied full process blank correction was less than 2%, except for THM-IS-T4-4 (3.4 %); consequently, the effect of ^{9}Be mis-estimation was excluded (see also Bender et al., 2016). Contributions of native Be, if present, were negligible because the total Be concentrations of the samples differed from the added spiked values within the uncertainties of the ICP-OES. Total Al concentrations varied between 0.45 and 20.03 mg (7 to 197 ppm). ^{26}Al/^{10}Be ratios changed from 2.50 ± 0.09 to 19.73 ± 1.39. The isochron burial ages were calculated according to the steps described in detail in Erlanger et al. (2012) by using the MATLAB® script provided by Darryl Granger (personal communication). Our modeling yielded isochron slopes and isochron burial ages of 3.56 ± 0.23 and 1.4 ± 0.1 Ma for strath terrace T2 (Tables 2 and 3; Fig. 10a) and 5.26 ± 0.23 and 540 ± 90 ka for the aggradational terrace T1 (Tables 2 and 3; Fig. 10b), respectively. Modeling of the results from the samples from strath terrace T1 did not yield any solution (Fig. 10c). We can explain this by the high ^{26}Al/^{10}Be ratios (>8.4, after Akçar et al., 2017) in the three samples from this terrace (Tables 2 and 3).

Sample depth, amount of dissolved samples, and added ^{35}Cl spikes are presented in Table 4, as well as the total Cl and ^{36}Cl concentrations and their 1-σ uncertainties. We analyzed one sample per depth profile (THM-DP-T2-4) for major and trace elements, which were taken as representative for the respective profile (Table S2). Total Cl concentrations for the five samples from the terrace were between 60 and 205 ppm (Table 4). ^{36}Cl concentrations varied from $(132.03 \pm 3.71) \times 10^4$ to $(240.97 \pm 9.47) \times 10^4$ atoms per gram rock (Table 4). The uncertainties from the AMS measurements fell between 2 and 5%. The input parameters for the modeling of the depth profile ages of the aggradational terrace T1 are given in Table S3. For the aggradational terrace T1, an independent cosmogenic ^{36}Cl modal age of 400^{+150}_{-50} ka, an inheritance of $(79^{+312}_{-79}) \times 10^4$ atoms/g, and an erosion rate of $0.34^{+0.30}_{-0.19}$ cm/ka were obtained from the simulation within 4 sigma (σ) (Fig. 10d; Table 5). The best fit through the data points using the lowest $\chi 2$ value generated an age of 300 ka, an inheritance of 2×10^4 atoms/g, and an erosion rate of 0.34 cm/ka (Fig. 11d).

The aggradation time of terrace T1 at 540 ± 90 ka (1 σ) and the timing of terrace formation at 400^{+150}_{-50} ka (4σ) agreed well within the uncertainties. Therefore, we consider 540 ± 90 ka (1 σ) as the age of T1 and the isochron burial age of 1.4 ± 0.1 Ma for T2 for further discussion. We used these ages to calculate the mean incision rate, i.e., isochron burial ages were plotted against the height of the terraces T1 and T2 with respect to present level of the Tohma River. The regression lines for the long-term incision rates (since 1.4 Ma) according to present level yielded a mean incision rate of 96 ± 11 m/Ma (Fig. 10e).

4.3. Uplift and Displacement

The difference in topographic elevation between the sampled locations of the terrace levels and the modern Tohma River was the first input to calculate the incision rate. The cross-section of P1 indicated that the mean sampling location of T2 was 106 m above the Tohma River (Fig. 7a) and that of P2 indicated that the mean sampling location was 28 m above (Fig. 7b). To calculate incision rates, we took into account the ratio of terrace heights to their isochron burial ages. According to this, the incision rates from T1 and T2 were found to be 0.052 ± 0.01 mm/yr and 0.076 ± 0.05 mm/yr, respectively. The plotting of the burial ages against the height of the terraces with respect to the modern elevation of the Tohma River was used to calculate the mean incision rate. The linear regression (after Bender et al., 2016) for the long-term incision rate (since 1.4 Ma) according to present level yielded a value of 96 ± 11 m/Ma (Fig. 10e).

The difference in the width of the Tohma River Valley on either side of the fault is the result of the lateral erosion that can be attributed to different lithologies across the river. The narrow and deep Tohma Valley, west of the Malatya Fault, is located on erosion-resistant limestone and consolidated volcaniclastic pebbles of the Medik Formation. In this area, the width of the modern channel is ca. 185 m (Fig. 3). After crossing the Malatya Fault (east of the fault), the valley presents a wider geometry as a result of relatively more erodible Plio–Quaternary units. In Fig. 3, the modern channel width between the fault and the black dashed line reaches up to 500 m whereas to the east of the white line the width reaches up to 1400 m (Fig. 3).

For the offset measurements on the Tohma River, we produced two scenarios. In the first offset scenario, we considered present channel boundaries at both sides of the fault. To measure the actual displacement based on the channels, we applied the criteria of Huang (1993) that define how fault displacement can be determined from the different types of deflection configurations. In Type-1, actual offset (D) can be measured easily because there is no apparent

displacement (Fig. 11a) (Huang, 1993). Type-II and Type-III have apparent displacement (D') that is caused by stream incision and lateral erosion (Figs. 11b and c) (Huang, 1993). The resulting channel geometry is either convex or concave along the fault strike. These misalignments create apparent displacement (D'). Therefore, to measure the actual displacement (D), the convex and concave segments of the river must be ignored. In Type-IV, stream channel behave like a brittle string and is abruptly offset within the narrow fault zone (Fig. 11d) (Huang, 1993). The configuration of the Tohma River near the Malatya Fault (Fig. 11e) is similar to the Type-II and Type-III of Huang (1993). We took into account the northern boundaries of the Tohma modern channel at both sides of the fault and measured the actual offset as 697 ± 1 m.

In the second offset scenario, we considered the present channel boundary at the western block of the fault and the oldest channel boundary at the eastern block of the fault, as presented by the oldest terrace (T2). We took into account the northern boundaries of the Tohma modern channel west of the fault, and to the east we considered the minimum and maximum boundary of T2 terraces (L1 and L2 lines in Fig. 11f). According to these reconstructions we measured 1411 ± 1 m and 1563 ± 1 m offsets (Fig. 11f).

5. Discussion

5.1. Quaternary Activity of the Malatya Fault

The dating of the Tohma terraces provided valuable data that were used to calculate the uplift rate. Since the long profile of Tohma is away from the effect of sea level fluctuations, we therefore, assumed that net incision equal to net uplift. The calculated incision rates of the T1

and T2 terraces were 0.052 ± 0.01 mm/yr and 0.076 ± 0.05 mm/yr, respectively. Considering the spatial distribution of the terraces and their relationship with the Malatya Fault, we propose that the uplift has been driven by the Malatya Fault rather than large-scale lithospheric processes, climatic effects, or sea level fluctuations. The calculated 96 ± 11 m/Ma mean uplift rate since at least 1.4 ± 0.1 Ma (Fig. 11d) is ca. 2 times larger than 51 ± 1 m/Ma from the central part of the Anatolian *Scholle*, where the uplift rate was estimated from Kızılırmak terraces (Çiner et al., 2015).

We used two geomorphic markers, namely, the present channel boundary of the Tohma River west of the fault and the T2 terraces that are considered to represent the oldest channel boundary east of the fault, to produce the offset scenarios of the FS-3 segment of the MF (Fig. 11). The displacement measurements of the scenarios were based on projections of these geomorphic marker lines into the FS-3 trace that shows clear recent slip related structures (Fig. 5). According to the first reconstruction scenario, which presents the minimum offset estimate, the sinistral offset between the present channel boundary of the Tohma River at both sides of the fault was measured as 697 m (Fig. 11e). However, with the second reconstruction scenario, which is the maximum estimate, the results revealed that the sinistral offset between the geomorphic markers was either 1411 m or 1563 m (Fig. 11f). These offset estimates divided by 1.4±0.1 Ma for the T2 terraces age, yields a 0.5 ± 0.1 mm/yr slip rate for the first scenario, and 1.0 ± 0.01 mm/yr and 1.12 ± 0.01 mm/yr minimum and maximum slip rates for the second scenario, respectively. Considering the 2275 ± 605 yr earthquake recurrence interval of the Malatya Fault that produced four earthquakes over the last 10 ka (Sançar et al., 2019), we conclude that the slip rate estimations from the second scenario are more plausible. Furthermore,

these estimations are consistent with one of the GPS-based block model slip rates, specifically, 1.2±0.1 mm/yr (Aktuğ et al., 2013a).

5.2. Quaternary Activity of Second-Order Strike-Slip Faults and Implications for Intra-Plate Deformation of the Eastern Part of the Anatolian *Scholle*

The studies on the strike-slip faults at the eastern part of the Anatolian *Scholle* unquestionably show that they are active structures, and apart from this, their slip rate, earthquake recurrence time, and tectonic evolution provide key data to discuss their origin and relationship with the westward extrusion of the *Anatolian Scholle*.

The westward extrusion rate of the Anatolian *Scholle* with respect to the Eurasian plate, increases from east to west, and the main deformation is accommodated by its boundary strike-slip faults (McClusky et al., 2000; Özeren and Holt, 2010; Reilinger et al., 2006; Şengör et al., 1985). Different hypotheses have been put forth to explain the causes for the westward motion of the Anatolian *Scholle*, including (a) the effect of the NAFZ and EAFZ supported by extra forces applied to Anatolia from beneath or forces from the gravitational potential of the East Anatolia High Plateau that is known as tectonic escape (McKenzie, 1972; Özeren and Holt, 2010; Şengör et al., 1985), (b) slab pull of the Hellenic subduction (Chorowicz et al., 1999; Reilinger et al., 2006), (c) asthenospheric flow dragging the circular motion of the lithosphere from the Levant in the east to Anatolia and Aegean in the west (Le Pichon and Kreemer, 2010), and (d) a combination of the effects of slab pull with mantle upwelling underneath Afar and with the large-scale flow associated with a whole mantle, Tethyan convection cell (Faccenna et al., 2013).

To evaluate these hypotheses by using the intra-plate deformational structures of the Anatolian *Scholle*, the origin and evolution of second-order strike-slip faults must be well established. Şengör et al. (1985) asserted that the paleotectonic structures have essential contributions regarding the formation of neotectonic structures and classified them into the following three groups according to their relationship with the paleotectonic structures: (a) *Resurrected structures:* these are formed by the reactivation of paleotectonic structures, (b) *Replacement structures:* the neotectonic structures are derived from the paleotectonic structures that are in the same spatial location, but their functions are different (e.g. the forming of the strike-slip fault as a result of a rotated suture), and (c) *Revolutionary structures:* these are not associated with the paleotectonic structures. Later studies on the CAFZ (Higgins et al., 2015; Koçyiğit and Beyhan, 1998), MOFZ (Kaymakçı et al., 2006), and TGFZ (Çemen et al., 1999; Özsayın et al., 2013) revealed that these faults originated from the paleotectonic structures during the late Miocene–early Pliocene. Considering their relationship with the paleotectonic structures, we think that they correspond to the replacement structures of Şengör et al. (1985); moreover, we assert that their replacement age is compatible with the age of the EAFZ (Arpat and Şaroğlu, 1972; Dewey et al., 1986; Hempton, 1987; Lyberis et al., 1992; Perinçek and Çemen, 1990; Şengör et al., 1985), which marks fully the development of the boundary faults of the Anatolian *Scholle* and therefore the beginning of its westward motion. A more recent study on Miocene to Pleistocene basaltic emplacement at the easternmost part of the Anatolian *Scholle* revealed supportive evidence that constrained the beginning of the westward motion (Di Giuseppe et al., 2017). Di Giuseppe et al. (2017) concluded that the westward motion of the Anatolian *Scholle*, which started after the development of the EAFZ at ca. 6 Ma ago, caused the formation of small pull-apart basins that facilitated the reaching of the Na-alkali basaltic magma

to the surface in the Plio–Pleistocene. Moreover, considering the slip rates and earthquake recurrence time, Sançar et al. (2019) proposed that these second-order strike-slip faults are plate boundary related structures. These data corroborate the ideas of Şengör et al. (1985), who suggested that simultaneous activity of the NAFZ and EAFZ caused the formation of the second-order strike-slip faults at the eastern part of the Anatolian *Scholle.*

Şengör (1979) and Şengör et al. (1985) suggested that an active Prandtl Cell model could be used to interpret the origin of intra-plate deformation of the Anatolian *Scholle* in the context of a tectonic escape model, but following a recent analogue model study, (Sançar et al., 2018) suggested that the passive wedge-shaped Prandtl cell model of Varnes (1962) is more appropriate for explaining the deformation pattern at the easternmost part of the Anatolian *Scholle*. Sançar et al. (2018) showed that the sense of slip along second-order faults, which formed between the NAFZ and EAFZ, changes along strike, from strike-slip to oblique normal and then to pure normal slip. Therefore, we think that the extensional structures on the CAFZ and MOFZ, or the increasing normal displacement along the southern part of the CAFZ, do not necessarily indicate the influence of the West Anatolian Extensional Province as proposed by Higgins et al. (2015).

6. Conclusions

The findings of this study provide a noteworthy contribution to the understanding of the spatio-temporal behavior of the Malatya Fault. These findings also enhance our understanding

of strike-slip faults in the eastern part of the Anatolian *Scholle*, which play a critical role in our understanding of geodynamics of the eastern Mediterranean region.

Isochron burial and depth profile dating of the Tohma River remnant terrace constrains the mid-Pleistocene slip and average uplift rate on the Malatya Fault. We produced two scenarios to measure actual offset between the present channel boundary in the west and the oldest channel boundary, which is represented by the T2 terrace level, east of the Malatya Fault. The 1.4 ± 0.1 Ma T2 terrace offset by ca. 1.4 km or ca. 1.5 km had respective slip rates of 1.0 ± 0.01 mm/yr and 1.12 ± 0.01. Furthermore, we calculated 0.052 ± 0.01 mm/yr and 0.076 ± 0.05 mm/yr incision rates for T1 and T2, respectively. According to the present level of the Tohma River the mean rock uplift rate for this segment of the Malatya Fault is 96 ± 11 m/Ma.

The reactivation period of intra-plate faults of the Anatolian *Scholle* corresponds fully to the development of the boundaries between the Anatolian *Scholle* and African and Arabian plates at ca. 6 Ma ago. The tectonic evolutions, slip rates, and earthquake recurrences of the main neotectonic structures of the eastern part of the Anatolian *Scholle* indicate that they have been controlled by the NAFZ and EAFZ, and this supports the tectonic escape model.

Acknowledgments

This study was supported by the TÜBİTAK grant no. 114Y580. Some figures in this paper were generated by using the public domain Generic Mapping Tools (GMT) software (Wessel et al., 2013).

References

Akçar, N., 2006. Paleoglacial records from the black sea area of Turkey: field and dating evidence [PhD: Bern University.

Akçar, N., Deline, P., Ivy-Ochs, S., Alfimov, V., Hajdas, I., Kubik Peter, W., Christl, M., Schlüchter, C., 2012a. The AD 1717 rock avalanche deposits in the upper Ferret Valley (Italy): a dating approach with cosmogenic 10Be. J Quaternary Sci. 27, 383-392. https://doi.org/10.1002/jqs.1558

Akçar, N., Ivy-Ochs, S., Alfimov, V., Schlunegger, F., Claude, A., Reber, R., Christl, M., Vockenhuber, C., Dehnert, A., Rahn, M., Schlüchter, C., 2017. Isochron-burial dating of glaciofluvial deposits: First results from the Swiss Alps. Earth Surf Proc Land.42, 2414-2425. https://doi.org/10.1002/esp.4201

Akçar, N., Tikhomirov, D., Özkaymak, Ç., Ivy-Ochs, S., Alfimov, V., Sözbilir, H., Uzel, B., Schlüchter, C., 2012b. 36Cl exposure dating of paleoearthquakes in the Eastern Mediterranean: First results from the western Anatolian Extensional Province, Manisa fault zone, Turkey. Geol Soc Am Bull.124, 1724-1735. https://doi.org/10.1130/B30614.1

Aktuğ, B., Dikmen, U., Dogru, A., Ozener, H., 2013a. Seismicity and strain accumulation around Karliova Triple Junction (Turkey). J Geodyn. 67, 21-29. http://dx.doi.org/10.1016/j.jog.2012.04.008

Aktuğ, B., Parmaksız, E., Kurt, M., Lenk, O., Kılıçoğlu, A., Gürdal, M. A., Özdemir, S., 2013b. Deformation of Central Anatolia: GPS implications: J Geodyn. 67, 78-96. https://doi.org/10.1016/j.jog.2012.05.008

Akyüz, H. S., Altunel, E., Karabacak, V., Yalçıner, C. Ç., 2006. Historical earthquake activity of the northern part of the Dead Sea Fault Zone, southern Turkey. Tectonophysics, 426, 281-293. https://doi.org/10.1016/j.tecto.2006.08.005

Akyüz, H. S., Uçarkus, G., Altunel, E., Doğan, B., Dikbaş, A., 2012. Paleoseismological investigations on a slow-moving active fault in central Anatolia, Tecer Fault, Sivas. Ann Geophys. 55, 847-857. https://doi.org/10.4401/ag-5444

Alfimov, V., Ivy-Ochs, S., 2009. How well do we understand production of 36Cl in limestone and dolomite? Quat Geochronol. 4, 462-474. https://doi.org/10.1016/j.quageo.2009.08.005

Anderson, R. S., Repka, J. L., Dick, G. S., 1996. Explicit treatment of inheritance in dating depositional surfaces using in situ 10Be and 26Al. Geology, 24, 47-51. https://doi.org/10.1130/0091-7613(1996)024<0047:ETOIID>2.3.CO;2

Arpat, E., Şaroğlu, F., 1972. Dogu Anadolu fayı ile ilgili bazı gözlem ve düşünceler (Some observations and thoughts on the East Anatolian fault): MTA Dergisi, 73 44–50.

Arpat, E., Şaroğlu, F., 1975. Türkiye'deki bazı önemli genç tektonik olaylar (On some important young tectonic events in Turkey): Bulletin of the Geological Society of Turkey, 18, 29–41.

Avagyan, A., Sosson, M., Karakhanian, A., Philip, H., Rebai, S., Rolland, Y., Melkonyan, R., and Davtyan, V., 2010. Recent tectonic stress evolution in the Lesser Caucasus and adjacent regions. Geol Soc Spec Publ, London. 340, 393. https://doi.org/10.1144/SP340.17

Balco, G., Rovey, C. W., 2008. An isochron method for cosmogenic-nuclide dating of buried soils and sediments. Am J Sci. 308, 1083-1114. https://doi.org/10.2475/10.2008.02

Balco, G., Soreghan, G. S., Sweet, D. E., Marra, K. R., Bierman, P. R., 2013. Cosmogenic-nuclide burial ages for Pleistocene sedimentary fill in Unaweep Canyon, Colorado, USA. Quat Geochronol. 18, 149-157. https://doi.org/10.1016/j.quageo.2013.02.002

Bedi, Y., Yusufoğlu, H., 2018. 1/100.000 ölçekli Türkiye Jeoloji Hatitaları Serisi, Malatya L40 Paftası, No:61.

Bedi, Y., Yusufoğlu, H., Beyazprinç, M., Usta, D., Yıldız, H., 2009. Doğu Torosların Jeodinamik Evrimi (Afşin-Elbistan-Göksun-Sarız dolayı): Maden Tetkik ve Arama Genel Müdürlüğü, Rapor No:11150.

Bender, A., M., Amos, C., B., Bierman, P., Rood, D., H., Staisch, L., Kelsey, H., Sherrod, B., 2016. Differential uplift and incision of the Yakima River terraces, central Washington State. J Geophys Res-Solid. 121, 365-384. https://doi.org/10.1002/2015JB012303

Borchers, B., Marrero, S., Balco, G., Caffee, M., Goehring, B., Lifton, N., Nishiizumi, K., Phillips, F., Schaefer, J., and Stone, J., 2016, Geological calibration of spallation production rates in the CRONUS-Earth project. Quat Geochronol. 31, 188-198. https://doi.org/10.1016/j.quageo.2015.01.009

Bozkurt, E., 2001. Neotectonics of Turkey; a synthesis. Geodin Acta. 14, 3-30. https://doi.org/10.1016/S0985-3111(01)01066-X

Bridgland, D. R., 2000. River terrace systems in north-west Europe: an archive of environmental change, uplift and early human occupation. Quaternary Sci Rev. 19, 1293-1303. https://doi.org/10.1016/S0277-3791(99)00095-5

Çemen, İ., Göncüoglu, M. C., Dirik, K., 1999. Structural Evolution of the Tuzgölü Basin in Central Anatolia, Turkey. J Geol. 107, 693-706. https://doi.org/10.1086/314379

Chmeleff, J., von Blanckenburg, F., Kossert, K., Jakob, D., 2010. Determination of the 10Be half-life by multicollector ICP-MS and liquid scintillation counting. Nuclear Instruments and Methods in Physics Research Section B: Beam Interactions with Materials and Atoms, 268, 192-199. https://doi.org/10.1016/j.nimb.2009.09.012

Chorowicz, J., Dhont, D., Gündogdu, N., 1999. Neotectonics in the eastern North Anatolian fault region (Turkey) advocates crustal extension: mapping from SAR ERS imagery and Digital Elevation Model. J Struct Geol. 21, 511-532. https://doi.org/10.1016/S0191-8141(99)00022-X

Christl, M., Vockenhuber, C., Kubik, P. W., Wacker, L., Lachner, J., Alfimov, V., Synal, H. A., 2013. The ETH Zurich AMS facilities: Performance parameters and reference materials: Nuclear Instruments and Methods in Physics Research Section B: Beam Interactions with Materials and Atoms, 294, 29-38. https://doi.org/10.1016/j.nimb.2012.03.004

Çiner, A., Doğan, U., Yıldırım, C., Akçar, N., Ivy-Ochs, S., Alfimov, V., Kubik, P. W., Schlüchter, C., 2015. Quaternary uplift rates of the Central Anatolian Plateau, Turkey: insights from cosmogenic

isochron-burial nuclide dating of the Kızılırmak River terraces. Quaternary Sci Rev. 107, 81-97. http://dx.doi.org/10.1016/j.quascirev.2014.10.007

Claude, A., Akçar, N., Ivy-Ochs, S., Schlunegger, F., Kubik, P. W., Christl, M., Vockenhuber, C., Kuhlemann, J., Rahn, M., Schlüchter, C., 2019. Changes in landscape evolution patterns in the northern Swiss Alpine Foreland during the mid-Pleistocene revolution. Geol Soc Am Bull. https://doi.org/10.1130/B31880.1

Darling, A. L., Karlstrom, K. E., Granger, D. E., Aslan, A., Kirby, E., Ouimet, W. B., Lazear, G. D., Coblentz, D. D., Cole, R. D., 2012. New incision rates along the Colorado River system based on cosmogenic burial dating of terraces: Implications for regional controls on Quaternary incision. Geosphere, 8, 1020-1041. https://doi.org/10.1130/GES00724.1

Desilets, D., Zreda, M., Almasi, P. F., Elmore, D., 2006. Determination of cosmogenic 36Cl in rocks by isotope dilution: innovations, validation and error propagation. Chem Geol. 233, 185-195. https://doi.org/10.1016/j.chemgeo.2006.03.001

Dewey, J. F., Hempton, M. R., Kidd, W. S. F., Şaroğlu, F., Şengör, A. M. C., 1986. Shortening of continental lithosphere: The neotectonics of Eastern Anatolia – a young collision zone. In: Coward, M. P., and Ries, A. C. (Eds.), Collision Tectonics, Volume 19: London, Geol Soc Spec Publ. pp. 3-36. https://doi.org/10.1144/GSL.SP.1986.019.01.01

Dewey, J. F., Şengör, A. M. C., 1979. Aegean and surrounding regions: Complex multiplate and continuum tectonics in a convergent zone. Geol Soc Am Bull. 90, 84-92. https://doi.org/10.1130/0016-7606(1979)90<84:AASRCM>2.0.CO;2

Di Giuseppe, P., Agostini, S., Lustrino, M., Karaoğlu, Ö., Savaşçın, M. Y., Manetti, P., Ersoy, Y., 2017. Transition from Compression to Strike-slip Tectonics Revealed by Miocene–Pleistocene Volcanism West of the Karlıova Triple Junction (East Anatolia). J Petrol 58, 2055-2087. https://doi.org/10.1093/petrology/egx082

Dirik, K., Göncüoglu, M. C., 1996. Neotectonic Characteristics of Central Anatolia: Int Geol Rev. 38, 807-817. https://doi.org/10.1080/00206819709465363

Duman, T. Y., Çan, T., Emre, Ö., Kadirioğlu, F. T., Başarır Baştürk, N., Kılıç, T., Arslan, S., Özalp, S., Kartal, R. F., Kalafat, D., Karakaya, F., Eroğlu Azak, T., Özel, N. M., Ergintav, S., Akkar, S., Altınok, Y., Tekin, S., Cingöz, A., Kurt, A. İ., 2017. Türkiye Sismotektonik Haritası, Özel Yayın Serisi-34, Maden Tetkik Arama Genel Müdürlüğü, Ankara-Türkiye.

Duman, T. Y., Emre, Ö., 2013. The East Anatolian Fault: geometry, segmentation and jog characteristics. In: Robertson, A. H. F., Parlak, O., and Ünlügenç,, U. C., (Eds.), Geological Development of Anatolia and the Easternmost Mediterranean Region. Volume 372: London, Geol Soc Spec Publ. pp. 495-529. https://doi.org/10.1144/SP372.14

Ekström, G., Nettles, M., Dziewoński, A. M., 2012. The global CMT project 2004–2010: Centroid-moment tensors for 13,017 earthquakes. Phys Earth Planet In.200-201, 1-9. https://doi.org/10.1016/j.pepi.2012.04.002

Elmore, D., Ma, X., Miller, T., Mueller, K., Perry, M., Rickey, F., Sharma, P., Simms, P., Lipschutz, M., Vogt, S., 1997. Status and plans for the PRIME Lab AMS facility. Nuclear Instruments and Methods in Physics Research Section B: Beam Interactions with Materials and Atoms, 123, 69-72. https://doi.org/10.1016/S0168-583X(96)00621-0

Emre, Ö., Duman, T. Y., Elmacı, H., Özalp, S., Olgun, Ş., 2012a. 1:250.000 Ölçekli Türkiye Diri Fay HaritasıSerisi, Malatya (NJ 37-6) Paftası, Seri No:42.

Emre, Ö., Duman, T. Y., Olgun, Ş., Elmacı, H., . Özalp, S., 2012b. 1:250.000 Ölçekli Türkiye Diri Fay Haritası Serisi, Divriği (NJ 37-2) Paftası, Seri No:41.

Ercan, S., 2011, Malatya Havzasında yer alan Beylerderesi Formasyonu'nun sedimantolojisi ve stratigrafisi: Çukurova Üniversitesi, Fen Bilimleri Enstitüsü, Yüksek Lisans Tezi-unpublished.

Erlanger, E. D., Granger, D. E., Gibbon, R. J., 2012. Rock uplift rates in South Africa from isochron burial dating of fluvial and marine terraces: Geology, 40, 1019-1022. https://doi.org/10.1130/G33172.1

Evans, J. M., Stone, J. O. H., Fifield, L. K., Cresswell, R. G., 1997. Cosmogenic chlorine-36 production in K-feldspar: Nuclear Instruments and Methods in Physics Research Section B: Beam Interactions with Materials and Atoms, 123, 334-340. https://doi.org/10.1016/S0168-583X(96)00714-8

Faccenna, C., Becker, T. W., Jolivet, L., Keskin, M., 2013. Mantle convection in the Middle East: Reconciling Afar upwelling, Arabia indentation and Aegean trench rollback. Earth Planet Sc Lett. 375, 254-269. http://dx.doi.org/10.1016/j.epsl.2013.05.043

Faccenna, C., Bellier, O., Martinod, J., Piromallo, C., Regard, V., 2006. Slab detachment beneath eastern Anatolia: A possible cause for the formation of the North Anatolian fault. Earth Planet Sc Lett. 242, 85-97. https://doi.org/10.1016/j.epsl.2005.11.046

Fink, D., Vogt, S., Hotchkis, M., 2000. Cross-sections for 36Cl from Ti at Ep=35–150 MeV: Applications to in-situ exposure dating: Nuclear Instruments and Methods in Physics Research Section B: Beam Interactions with Materials and Atoms, 172, 861-866. https://doi.org/10.1016/S0168-583X(00)00200-7

Görür, N., Oktay, F. Y., Seymen, İ., Şengör, A. M. C., 1984. Palaeotectonic evolution of the Tuzgölü basin complex, Central Turkey: sedimentary record of a Neo-Tethyan closure. Geol Soc Spec Publ, London. 17, 467. https://doi.org/10.1144/GSL.SP.1984.017.01.34

Gosse, J. C., Phillips, F. M., 2001. Terrestrial in situ cosmogenic nuclides: theory and application: Quaternary Sci Rev. 20, 1475-1560. http://dx.doi.org/10.1016/S0277-3791(00)00171-2

Granger, D. E., 2006. A review of burial dating methods using 26Al and 10Be. In: Alonso-Zarza, A. M., and Tanner, L. H., (Eds.), In Situ-Produced Cosmogenic Nuclides and Quantification of Geological Processes, Geological Society of America. https://doi.org/10.1130/2006.2415(01)

Gürbüz, K., Gül, M., 2005. Evolution of and Factors Controlling Eocene Sedimentation in the Darende-Balaban Basin, Malatya (Eastern Turkey). Turk J Earth Sci.14, 311-335.

Gürsoy, H., Piper, J. D. A., Tatar, O., Temiz, H., 1997. A palaeomagnetic study of the Sivas Basin, central Turkey: Crustal deformation during lateral extrusion of the Anatolian Block. Tectonophysics, 271, 89-105. https://doi.org/10.1016/S0040-1951(96)00242-9

Gürsoy, H., Tatar, O., Piper, J. D. A., Koçbulut, F., AkpInar, Z., Huang, B., Roberts, A. P., Mesci, B. L., 2011. Palaeomagnetic study of the Kepezdag and Yamadag volcanic complexes, central Turkey: Neogene tectonic escape and block definition in the central-east Anatolides. J Geodyn.51, 308-326. https://doi.org/10.1016/j.jog.2010.07.004

Hakyemez, T., Örçen, S., 1982. Medik-Eberme dolayındaki (Malatya kıuzeybatısı) Senozoyik yaşlı çökel kayaların stratigrafisi ve sedimantolojisi. Maden Tetkik ve Arama Enstitüsü Rapor No:7213, Ankara (unpublished).

Hall, J., Aksu, A. E., Elitez, I., Yaltırak, C., Çifçi, G., 2014. The Fethiye–Burdur Fault Zone: A component of upper plate extension of the subduction transform edge propagator fault linking Hellenic and Cyprus Arcs, Eastern Mediterranean. Tectonophysics, 635, 80-99. https://doi.org/10.1016/j.tecto.2014.05.002

Hancock, G. S., Anderson, R. S., Chadwick, O. A., Finkel, R. C., 1999. Dating fluvial terraces with 10Be and 26Al profiles: application to the Wind River, Wyoming. Geomorphology, 27, 41-60. http://dx.doi.org/10.1016/S0169-555X(98)00089-0

Hempton, M. R., 1987. Constraints on Arabian plate motion and extensional history of the Red Sea. Tectonics, 153, 687-705. https://doi.org/10.1029/TC006i006p00687

Hidy, A. J., Gosse, J. C., Pederson, J. L., Mattern, J. P., Finkel, R. C., 2010. A geologically constrained Monte Carlo approach to modeling exposure ages from profiles of cosmogenic nuclides: An

example from Lees Ferry, Arizona. Geochem Geophy Geosy. 11, https://doi.org/10.1029/2010GC003084

Higgins, M., Schoenbohm, L. M., Brocard, G., Kaymakci, N., Gosse, J. C., Cosca, M. A., 2015. New kinematic and geochronologic evidence for the Quaternary evolution of the Central Anatolian fault zone (CAFZ). Tectonics, 34, 2118-2141. https://doi.org/10.1002/2015TC003864

Huang, W., 1993. Morphologic patterns of stream channels on the active Yishi Fault, southern Shandong Province, Eastern China: Implications for repeated great earthquakes in the Holocene. Tectonophysics, 219, 283-304. https://doi.org/10.1016/0040-1951(93)90179-N

Hubert-Ferrari, A., King, G., Woerd, J. v. d., Villa, I., Altunel, E., Armijo, R., 2009. Long-term evolution of the North Anatolian Fault: new constraints from its eastern termination. Geol Soc Spec Publ, London. 311, 133-154. https://doi.org/10.1144/SP311.5

Ivy-Ochs, S., Schäfer, J., Kubik, P. W., Synal, H.-A., Schlüchter, C., 2004. Timing of deglaciation on the northern Alpine foreland (Switzerland). Eclogae Geol Helv. 97, 47-55. https://doi.org/10.1007/s00015-004-1110-0

Jackson, J., McKenzie, D., 1984. Active tectonics of the Alpine–Himalayan Belt between western Turkey and Pakistan. Geophys J Roy Astr S. 77, 185–264. https://doi.org/10.1111/j.1365-246X.1984.tb01931.x

Karaman, T., Poyraz, N., Bakırhan, B., Alan, İ., Kadınkız, G., Yılmaz, H., Kılınç, F., 1993. Malatya-Doğanşehir-Çelikhan dolayının jeolojisi. Maden Tetkik ve Arama Genel Müdürlüğü Rapor No:9587, Ankara (unpublished).

Kaymakçı, N., İnceöz, M., Ertepınar, P., 2006. 3D- Architecture and Neogene Evolution of the Malatya Basin: Inferences for the Kinematics of the Malatya and Ovacık Fault Zones. Turk J Earth Sci.15, 123-154.

Kaymakçı, N., Inceöz, M., Ertepinar, P., Koç, A., 2010. Late Cretaceous to Recent kinematics of SE Anatolia (Turkey). Geol Soc Spec Publ, London. 340, 409. https://doi.org/10.1144/SP340.18

Koçyiğit, A., Beyhan, A., 1998. A new intra-continental transcurrent structure: The Central Anatolian Fault Zone, Turkey. Tectonophysics, 284, 317-336. https://doi.org/10.1016/S0040-1951(97)00176-5

Kohl, C. P., Nishiizumi, K., 1992. Chemical isolation of quartz for measurement of in-situ-produced cosmogenic nuclides. Geochim Cosmochim Ac. 56, 3583-3587. https://doi.org/10.1016/0016-7037(92)90401-4

Korschinek, G., Bergmaier, A., Faestermann, T., Gerstmann, U. C., Knie, K., Rugel, G., Wallner, A., Dillmann, I., Dollinger, G., von Gostomski, C. L., Kossert, K., Maiti, M., Poutivtsev, M., Remmert, A., 2010. A new value for the half-life of 10Be by Heavy-Ion Elastic Recoil Detection and liquid scintillation counting. Nuclear Instruments and Methods in Physics Research Section B: Beam Interactions with Materials and Atoms, 268, 187-191. https://doi.org/10.1016/j.nimb.2009.09.020

Kubik, P. W., Christl, M., 2010. 10Be and 26Al measurements at the Zurich 6MV Tandem AMS facility. Nuclear Instruments and Methods in Physics Research Section B: Beam Interactions with Materials and Atoms, 268, 880-883. https://doi.org/10.1016/j.nimb.2009.10.054

Kürçer, A., Gökten, Y. E., 2012. Paleoseismological Three Dimensional Virtual Photography Method; A Case Study: Bağlarkayası-2010 Trench, Tuz Gölü Fault Zone, Central Anatolia, Turkey, *in* Sharkov, E., ed., Tectonics: Rijeka, InTech, pp. 201–228. http://dx.doi.org/10.5772/48194

Lal, D., 1991. Cosmic ray labeling of erosion surfaces: in situ nuclide production rates and erosion models. Earth Planet Sc Lett.104, 424-439. https://doi.org/10.1016/0012-821X(91)90220-C

Le Pichon, X., 1982. Land-locked oceanic basins and continental collision: the Eastern Mediterranean as a case example: Mountain building processes, p. 201-211.

Le Pichon, X., Chamot-Rooke, N., L., S., Noomen, R., Veis, G., 1995. Geodetic determination of the kinematics of central Greece with respect to Europe: Implications for eastern Mediterranean tectonics.J Geophys Res-Solid. 100, 12675-12690. https://doi.org/10.1029/95JB00317

Le Pichon, X., Kreemer, C., 2010. The Miocene-to-Present Kinematic Evolution of the Eastern Mediterranean and Middle East and Its Implications for Dynamics. Annu Rev Earth Pl Sc. 38, 323-351. https://doi.org/10.1146/annurev-earth-040809-152419

Liu, B. L., Phillips, F. M., Fabrykamartin, J. T., Fowler, M. M., Stone, W. D., 1994. Cosmogenic 36Cl accumulation in unstable landforms: 1. Effects of the thermal neutron distribution. Water Resour Res. 30, 3115-3125. https://doi.org/10.1029/94WR00761

Lyberis, N., Yürür, T., Chorowicz, J., Kasapoğlu, E.,Gündoğdu, N., 1992. The East Anatolian fault: an oblique collisional belt. Tectonophysics, 204, 1-15. https://doi.org/10.1016/0040-1951(92)90265-8

Maddy, D., Bridgland, D., Westaway, R., 2001. Uplift-driven valley incision and climate-controlled river terrace development in the Thames Valley, UK. Quatern Int. 79, 23-36. http://dx.doi.org/10.1016/S1040-6182(00)00120-8

McClusky , S., Balassanian, S., Barka, A., Demir, C., Ergintav, S., Georgiev, I., Gurkan, O., Hamburger, M., Hurst, K., Kahle, H., Kastens, K., Kekelidze, G., King, R., Kotzev, V., Lenk, O., Mahmoud, S., Mishin, A., Nadariya, M., Ouzounis, A., Paradissis, D., Peter, Y., Prilepin, M., Reilinger, R., Sanli, I., Seeger, H., Tealeb, A., Toksöz, M. N., Veis, G., 2000. Global Positioning System constraints on plate kinematics and dynamics in the eastern Mediterranean and Caucasus. J Geophys Res. 105, 5695-5719. https://doi.org/10.1029/1999JB900351

McKenzie, D., 1972. Active Tectonics of the Mediterranean Region. Geophys J Roy Astr S. 30, 109-185. https://doi.org/10.1111/j.1365-246X.1972.tb02351.x

McKenzie, D., 1978. Active tectonics of the Alpine—Himalayan belt: the Aegean Sea and surrounding regions. Geophys J Roy Astr S. 55, 217–254. https://doi.org/10.1111/j.1365-246X.1978.tb04759.x

Merritts Dorothy, J., Vincent Kirk, R., Wohl Ellen, E., 2012. Long river profiles, tectonism, and eustasy: A guide to interpreting fluvial terraces. J Geophys Res-Solid. 99, 14031-14050. https://doi.org/10.1029/94JB00857

Muehlberger, W. R., Gordon, M. B., 1987. Observations on the complexity of the east anatolian fault, Turkey. J Struct Geol.9, 899-903. https://doi.org/10.1016/0191-8141(87)90091-5

Nica, N., Cameron, J., Singh, B., 2012. Nuclear Data Sheets for A = 36. Nuclear Data Sheets, 113, 1-155. https://doi.org/10.1016/j.nds.2012.01.001

Nishiizumi, K., 2004. Preparation of 26Al AMS standards. Nuclear Inst. and Methods in Physics Research, 223-224, 388-392. https://doi.org/10.1016/j.nimb.2004.04.075

Norris, T. L., Gancarz, A. J., Rokop, D. J., Thomas, K. W., 1983. Half-life of Al-26. J Geophys Res. 88, B331-B333. https://doi.org/10.1029/JB088iS01p0B331

Nyst, M., Thatcher, W., 2004. New constraints on the active tectonic deformation of the Aegean. J Geophys Res-Solid. 109, https://doi.org/10.1029/2003JB002830

Özener, H., Arpat, E., Ergintav, S., Dogru, A., Cakmak, R., Turgut, B., Dogan, U., 2010. Kinematics of the eastern part of the North Anatolian Fault Zone. J Geodyn. 49, 141-150. http://dx.doi.org/10.1016/j.jog.2010.01.003

Özeren, M. S., Holt, W. E., 2010. The dynamics of the eastern Mediterranean and eastern Turkey. Geophys J Int. 183, 1165-1184. https://doi.org/10.1111/j.1365-246X.2010.04819.x

Özsayın, E., Çiner, A., Rojay, B., Dirik, K., Melnick, D., Fernandez-Blanco, D., Bertotti, G., Schildgen, T., Garcin, Y., Strecker, M., Sudo, M., 2013. Plio-Quaternary extensional tectonics of the Central Anatolian Plateau: a case study from the Tuz Gölü Basin, Turkey: Turk J Earth Sci.22, 691-714.

Öztürk, M. Z., Şener, M. F., Şener, M., Şahirner, E., 2018. Quaternary Slip-Rates of the Bor Segment of Tuzgölü Fault Zone. Omer Halisdemir University Journal of Engineering Sciences, 7, 1049-1053. https://doi.org/10.28948/ngumuh.502085

Pan, B., Su, H., Hu, Z., Hu, X., Gao, H., Li, J., Kirby, E., 2009. Evaluating the role of climate and tectonics during non-steady incision of the Yellow River: evidence from a 1.24Ma terrace record near Lanzhou, China. Quaternary Sci Rev. 28, 3281-3290. https://doi.org/10.1016/j.quascirev.2009.09.003

Pazzaglia, F. J., 2013. 9.22 Fluvial Terraces, *in* Shroder, J. F., ed., Treatise on Geomorphology: San Diego, Academic Press, pp. 379-412. http://dx.doi.org/10.1016/B978-0-12-374739-6.00248-7

Perinçek, D., Çemen, İ., 1990. The structural relationship between the East Anatolian and Dead Sea fault zones in southeastern Turkey. Tectonophysics, 172, 331-340. https://doi.org/10.1016/0040-1951(90)90039-B

Peters, G., van Balen, R. T., 2007. Pleistocene tectonics inferred from fluvial terraces of the northern Upper Rhine Graben, Germany. Tectonophysics, 430, 41-65. https://doi.org/10.1016/j.tecto.2006.10.008

Philip, H., Cisternas, A., Gvishiani, A., Gorshkov, A., 1989. The Caucasus: an actual example of the initial stages of continental collision. Tectonophysics, 161, 1-21. https://doi.org/10.1016/0040-1951(89)90297-7

Phillips, F. M., Stone, W. D., Fabryka-Martin, J. T., 2001. An improved approach to calculating low-energy cosmic-ray neutron fluxes near the land/atmosphere interface. Chem Geol. 175, 689-701. https://doi.org/10.1016/S0009-2541(00)00329-6

Phillips, F. M., Zreda, M., G., Flinsch, M., R., Elmore, D., Sharma, P., 1996. A reevaluation of cosmogenic 36Cl production rates in terrestrial rocks. Geophys Res Lett. 23, 949-952. https://doi.org/10.1029/96GL00960

Piper, J. D. A., Gürsoy, H., Tatar, O., Beck, M. E., Rao, A., Koçbulut, F., Mesci, B. L., 2010. Distributed neotectonic deformation in the Anatolides of Turkey: A palaeomagnetic analysis. Tectonophysics, 488, 31-50. https://doi.org/10.1016/j.tecto.2009.05.026

Reilinger, R., McClusky, S., Vernant, P., Lawrence, S., Ergintav, S., Cakmak, R., Ozener, H., Kadirov, F., Guliev, I., Stepanyan, R., Nadariya, M., Hahubia, G., Mahmoud, S., Sakr, K., ArRajehi, A., Paradissis, D., Al-Aydrus, A., Prilepin, M., Guseva, T., Evren, E., Dmitrotsa, A., Filikov, S. V., Gomez, F., Al-Ghazzi, R., Karam, G., 2006. GPS constraints on continental deformation in the Africa-Arabia-Eurasia continental collision zone and implications for the dynamics of plate interactions. J. Geophys. Res., 111, B05411. https://doi.org/10.1029/2005JB004051

Repka, J. L., Anderson, R. S., Finkel, R. C., 1997. Cosmogenic dating of fluvial terraces, Fremont River, Utah. Earth Planet Sc Lett. 152, 59-73. http://dx.doi.org/10.1016/S0012-821X(97)00149-0

Rolland, Y., Perincek, D., Kaymakci, N., Sosson, M., Barrier, E., Avagyan, A., 2012. Evidence for ~80–75Ma subduction jump during Anatolide–Tauride–Armenian block accretion and ~48Ma Arabia–Eurasia collision in Lesser Caucasus–East Anatolia. J Geodyn. 56-57, 76-85. https://doi.org/10.1016/j.jog.2011.08.006

Ruszkiczay-Rüdiger, Z., Braucher, R., Novothny, Á., Csillag, G., Fodor, L., Molnár, G., Madarász, B., 2016. Tectonic and climatic control on terrace formation: Coupling in situ produced 10Be depth profiles and luminescence approach, Danube River, Hungary, Central Europe. Quaternary Sci Rev. 131, 127-147. https://doi.org/10.1016/j.quascirev.2015.10.041

Sançar, T., Akyüz, H. S., Schreurs, G., Zabcı, C., 2018. Mechanics of plio-quaternary faulting around the Karliova triple junction: implications for the deformation of Eastern part of the Anatolian Scholle: Geodin Acta. 30, 287-305. https://doi.org/10.1080/09853111.2018.1533736

Sançar, T., Zabcı, C., Karabacak, V., Yazıcı, M., Akyüz, H. S., 2019. Geometry and Paleoseismology of the Malatya Fault (Malatya-Ovacık Fault Zone), Eastern Turkey: Implications for intraplate

deformation of the Anatolian Scholle. Journal of Seismology, 23, 319-340. https://doi.org/10.1007/s10950-018-9808-z

Sarıkaya, M. A., Yıldırım, C., Çiner, A., 2015. No surface breaking on the Ecemiş Fault, central Turkey, since Late Pleistocene (~64.5 ka); new geomorphic and geochronologic data from cosmogenic dating of offset alluvial fans. Tectonophysics, 649, 33-46. http://dx.doi.org/10.1016/j.tecto.2015.02.022

Seyitoğlu, G., Esat, K., Kaypak, B., 2017. The neotectonics of southeast Turkey, northern Syria, and Iraq: the internal structure of the Southeast Anatolian Wedge and its relationship with recent earthquakes. Turk J Earth Sci. 26, 105-126. https://doi.org/10.3906/yer-1605-21

Şaroğlu, F., Emre, Ö., Kuşçu, İ., 1992. Türkiye Diri Fay Haritasi (Active Faut Map of Turkey), scale 1:2000000, one sheet. Maden Tetkik ve Arama Genel Müdürlüğü.

Şaroğlu, F., Güner, Y., 1979. Tutak Diri Fayı, Özellikleri ve Çaldıran Fayı ile ilişkisi. Yeryuvarı ve İnsan, 4, 11-14.

Schimmelpfennig, I., Benedetti, L., Finkel, R., Pik, R., Blard, P.-H., Bourlès, D., Burnard, P., Williams, A., 2009. Sources of in-situ 36Cl in basaltic rocks. Implications for calibration of production rates. Quat Geochronol. 4, 441-461. https://doi.org/10.1016/j.quageo.2009.06.003

Searle, M. P., Chung, S.-L., Lo, C.-H., 2010. Geological offsets and age constraints along the northern Dead Sea fault, Syria. J Geol Soc London. 167, 1001-1008. https://doi.org/10.1144/0016-76492010-009

Şengör, A. M. C., 1979. The North Anatolian transform fault; its age, offset and tectonic significance. J Geol Soc London. 136, 269-282. https://doi.org/10.1144/gsjgs.136.3.0269

Şengör, A. M. C., 1980. Türkiye Neotektoniğinin Esasları (Principles of the Neotectonism of Turkey): Türkiye Jeoloji Kurumu Yayını, 40.

Şengör, A. M. C., Görür, N., Şaroğlu, F., 1985. Strike slip faulting and related basin formations in zones of tectonic escape: Turkey as a case study. In: Biddle, K. T., and Christie-Blick, N., (Eds.), Strike-Slip Faulting and Basin Formation, Society of Economic Paleontologists and Mineralogists, Tulsa, Oklahoma, Special Publication No. 37, pp. 227 – 264.

Şengör, A. M. C., Grall, C., İmren, C., Le Pichon, X., Görür, N., Henry, P., Karabulut, H., Siyako, M., 2014. The geometry of the North Anatolian transform fault in the Sea of Marmara and its temporal evolution: implications for the development of intracontinental transform faults. Can J Earth Sci. 51, 222-242. https://doi.org/10.1139/cjes-2013-0160

Şengör, A. M. C., Özeren, M. S., Keskin, M., SakInç, M., Özbakır, A. D., Kayan, I., 2008. Eastern Turkish high plateau as a small Turkic-type orogen: Implications for post-collisional crust-forming processes in Turkic-type orogens. Earth-Sci Rev. 90, 1-48. https://doi.org/10.1016/j.earscirev.2008.05.002

Şengör, A. M. C., Tüysüz, O., İmren, C., Sakınç, M., Eyidoğan, H., Görür, N., Le Pichon, X., Rangin, C., 2005. The North Anatolian Fault: A New Look: Annu Rev Earth Pl Sc. 33, 37-112. https://doi.org/10.1146/annurev.earth.32.101802.120415

Şengör, A. M. C., Yılmaz, Y., 1981. Tethyan evolution of Turkey: A plate tectonic approach. Tectonophysics, 75, 181-190, 193-199, 203-241. https://doi.org/10.1016/0040-1951(81)90275-4

Shaw, B., Jackson, J., 2010. Earthquake mechanisms and active tectonics of the Hellenic subduction zone. Geophys J Int. 181, 966-984. https://doi.org/10.1111/j.1365-246X.2010.04551.x

Stone, J. O., 2000. Air pressure and cosmogenic isotope production. J Geophys Res-Solid. 105, 23753-23759. https://doi.org/10.1029/2000JB900181

Stone, J. O., 2005. Terrestrial chlorine-36 production from spallation of iron, 10th International Conference on Accelerator Mass Spectrometry. Berkeley, California.

Stone, J. O., Allan, G. L., Fifield, L. K., Cresswell, R. G., 1996. Cosmogenic chlorine-36 from calcium spallation. Geochim Cosmochim Ac., 60, 679-692. https://doi.org/10.1016/0016-7037(95)00429-7

Stone, J. O. H., Evans, J. M., Fifield, L. K., Allan, G. L., Cresswell, R. G., 1998. Cosmogenic Chlorine-36 Production in Calcite by Muons. Geochim Cosmochim Ac., 62, 433-454. https://doi.org/10.1016/S0016-7037(97)00369-4

Sümengen, M., 2016. 1/100.000 ölçekli Türkiye Jeoloji Hatitaları Serisi, Malatya L40paftası, No:238, Maden Tetkik ve Arama Genel Müdürlüğü, Jeoloji Etütleri Dairesi, Ankara.

Synal, H. A., Bonani, G., Döbeli, M., Ender, R. M., Gartenmann, P., Kubik, P. W., Schnabel, C., Suter, M., 1997. Status report of the PSI/ETH AMS facility: Nuclear Instruments and Methods in Physics Research Section B: Beam Interactions with Materials and Atoms, 123, 62-68. https://doi.org/10.1016/S0168-583X(96)00608-8

Tatar, O., Poyraz, F., Gürsoy, H., Cakir, Z., Ergintav, S., Akpınar, Z., Koçbulut, F., Sezen, F., Türk, T., Hastaoğlu, K. Ö., Polat, A., Mesci, B. L., Gürsoy, Ö., Ayazlı, İ. E., Çakmak, R., Belgen, A., Yavaşoğlu, H., 2012. Crustal deformation and kinematics of the Eastern Part of the North Anatolian Fault Zone (Turkey) from GPS measurements. Tectonophysics, 518, 55-62. http://dx.doi.org/10.1016/j.tecto.2011.11.010

Uygun, A., Yaşar, M., Erkan, M. C., Baş, H., Çelik, E., Aygün, M., Bilgiç, T., Kayakıran, S., Ayok, F., 1982. Tuzgölü Havzası Projesi [Tuzgölü Basin Project].

Varnes, D. J., 1962. Analysis of plastic deformation according to Von Mises' theory, with application to the South Silverton area, San Juan County, Colorado. USGS Professional Paper, 378-B.

Wang, X., Vandenberghe, J., Yi, S., Van Balen, R., Lu, H., 2015. Climate-dependent fluvial architecture and processes on a suborbital timescale in areas of rapid tectonic uplift: An example from the

NE Tibetan Plateau. Global Planet Change. 133, 318-329. https://doi.org/10.1016/j.gloplacha.2015.09.009

Wessel, P., Smith, W. H. F., Scharroo, R., Luis, J., Wobbe, F., 2013. Generic Mapping Tools: Improved Version Released. Eos, Transactions American Geophysical Union, 94, 409-410. 10.1002/2013EO450001

Westaway, R., 1999. Comment on "A new intracontinental transcurrent structure: the Central Anatolian Fault Zone, Turkey" by A. Koçyiğit and A. Beyhan. Tectonophysics, 314, 469-479. http://dx.doi.org/10.1016/S0040-1951(99)00223-1

Westaway, R., Arger, J., 1996. The Gölbaşı basin, southeastern Turkey: a complex discontinuity in a major strike-slip fault zone J Geol Soc London. London, 153, 729– 744. https://doi.org/10.1144/gsjgs.153.5.0729

Westaway, R., Arger, J., 2001. Kinematics of the Malatya-Ovacik fault zone. Geodin Acta. 14, 103-131. https://doi.org/10.1016/S0985-3111(00)01058-5

Westaway, R., Demir, T., Seyrek, A., 2008. Geometry of the Turkey-Arabia and Africa-Arabia plate boundaries in the latest Miocene to Mid-Pliocene: the role of the Malatya-Ovacık Fault Zone in eastern Turkey. eEarth, 3, 27-35. https://doi.org/10.5194/ee-3-27-2008

Westaway, R., Demir, T., Seyrek, A., Beck, A., 2006. Kinematics of active left-lateral faulting in SE Turkey from offset Pleistocene river gorges: improved constraint on the rate and history of relative motion between the Turkish and Arabian plates. J Geol Soc London. 163, 149-164. https://doi.org/10.1144/0016-764905-030

Westaway, R. W. C., 2003. Kinematics of the Middle East and Eastern Mediterranean updated. Turk. J. Eart. Sci., 12, 5-46.

Yazıcı, M., Zabcı, C., Natal'in, B. A., Sançar, T., Akyüz, H. S., 2018a. Strike-slip deformation in a converging setting. Insights from the Ovacık Fault (Anatolia, Turkey), EGU General Assembly: Vienna, Austria. EGU2018-1052.

Yazıcı, M., Zabcı, C., Sançar, T., Natalin, B. A., 2018b. The role of intraplate strike-slip faults in shaping the surrounding morphology: The Ovacık Fault (eastern Turkey) as a case study. Geomorphology, 321, 129-145. https://doi.org/10.1016/j.geomorph.2018.08.022

Yıldırım, C., 2014. Relative tectonic activity assessment of the Tuz Gölü Fault Zone; Central Anatolia, Turkey. Tectonophysics, 630, 183-192. https://doi.org/10.1016/j.tecto.2014.05.023

Yıldırım, C., Sarıkaya, M. A., Çiner, A., 2016. Late Pleistocene intraplate extension of the Central Anatolian Plateau, Turkey: Inferences from cosmogenic exposure dating of alluvial fan, landslide, and moraine surfaces along the Ecemiş Fault Zone. Tectonics, 35, 1446-1464. https://doi.org/10.1002/2015TC004038

Zhao, Z., Granger, D., Zhang, M., Kong, X., Yang, S., Chen, Y., Hu, E., 2016. A test of the isochron burial dating method on fluvial gravels within the Pulu volcanic sequence, West Kunlun Mountains, China. Quat Geochronol. 34, 75-80. https://doi.org/10.1016/j.quageo.2016.04.003

URL, 2019. Deprem Detay https://deprem.afad.gov.tr/depremdetay?eventID=435078: Disaster & Emergency Management Authority Presidential of Earthquake Department, Ankara, Turkey. Last Access: 25.06.2019.

FIGURE CAPTIONS

Figure 1. (a) Major active tectonic structures of Turkey and the Eastern Mediterranean (Akyüz et al., 2006, 2012; Avagyan et al., 2010; Duman and Emre, 2013; Hall et al., 2014; Koçyiğit and Beyhan, 1998; Le Pichon et al., 1995; Nyst and Thatcher, 2004; Philip et al., 1989; Seyitoğlu et

al., 2017; Şaroğlu et al., 1992; Şaroğlu and Güner, 1979; Searle et al., 2010; Şengör et al., 1985, 2005, 2008, 2014; Shaw and Jackson, 2010). The red lines with saw teeth and hachures indicate the thrusts and normal faults, respectively. The red solid lines are strike-slip faults. KTJ: Karlıova Triple Junction, NAFZ: North Anatolian Fault Zone, EAFZ: East Anatolian Fault Zone, MOFZ: Malatya-Ovacık Fault Zone, CAFZ: Central Anatolian Fault Zone, TGFZ: Tuz Gölü Fault Zone, HT: Hellenic Trench, CT: Cyprus Trench. Basemap is from the GEBCO database (downloaded from http://www.gebco.net/data_and_products/gridded_bathymetry_data/). **(b)** The main active structures of central-to-eastern Turkey (Şaroğlu et al., 1992). Blue arrows indicate the GPS vectors (Aktuğ et al., 2013b; Özener et al., 2010; Reilinger et al., 2006; Tatar et al., 2012), focal mechanisms of the main earthquakes (M >5.5), which generally show strike-slip, and some normal fault solutions (Ekström et al., 2012). MF: Malatya Fault, OF: Ovacık Fault, TGB: Tuz Gölü Basin, EB: Erzincan Basin, E: Eynir.

Figure 2. The general geometry and segmentation of the 165-km-long NE–SW-striking Malatya Fault (modified from Emre et al., 2012a, b; Kaymakçı et al., 2006; Sançar et al., 2019). The white arrows indicate the segment boundaries (FS-1 to FS-5).

Figure 3. The simplified geologic map of the study area (modified from Bedi and Yusufoğlu, 2018; Sümengen, 2016). Note that the modern channel width of the Tohma River increase from west to east and reaches its maximum (1400 m) to the east of the white dashed line. The area west of the black dashed line shows the area in Fig. 6a. The area west of the black dashed line shows the area in Fig. 6a.

Figure 4. (a) Field view of the Beylerderesi Formation that is represented by poorly sorted limestone and basalt fragments, and **(b)** cross-lamination structure of the terrace deposits that reflect the fluvial deposition.

Figure 5. Physiographic features of the Malatya Fault at locations north and south of the Tohma River. **(a)** The elongated depression (between black arrows) on the crest line and **(b)** offset gullies were used to draw the fault geometry.

Figure 6. (a) Detailed geologic map (modified from Bedi and Yusufoğlu, 2018; Sümengen, 2016), and remnant terrace distribution around the Malatya Fault. **(b)** Close view of the T1 and T2 terraces to the south of the Tohma River showing the cosmogenic isochron burial (THM-IS-T2, T4 and PQ) and cosmogenic depth profile sampling (THM-DP-T2) locations. P1 and P2 swath profiles are shown in Fig. 7.

Figure 7. Swath profiles of **(a)** P1 and **(b)** P2 showing the sampling locations and their elevations from the Tohma River. See Fig. 6 for cross-section locations.

Figure 8. (a) The highest point of the T2 terrace (106 m above the thalweg of the Tohma Valley) sampled for cosmogenic isochron-burial dating **(b)** close view of the THM-IS-T4 site

Figure 9. Field pictures of the T1 terrace. **(a)** Sampling site of the T1 terrace. Blue dashed line presents the boundary of the T1 terrace at points south of the Tohma River. The black arrow shows the T1 terrace, covered with apricot trees, at points north of the river. **(b)** The 11 microcrystalline quartz pebble samples (THM-IS-T2-1 to 11) collected from the T1 aggradational terrace, and **(c)** THM-IS-PQ-1 to 7 samples collected from the T1 strath terrace for cosmogenic isochron burial dating. **(d)** The excavated trench (c.a. 2 m) on the T1 aggradational terrace sampled (THM-DP-T2-1 to 4) for cosmogenic depth profile dating.

Figure 10. Corrected isochron age for samples **(a)** THM-IS-T4, **(b)** THM-IS-T2, **(c)** THM-IS-PQ. **(d)** The best fit of depth profile dating of the THM-DP-T2 samples **(e)** Strath elevations of

the T2 and T4 terraces plotted against the terrace age. The slope of the solid line and its intercept are used to calculate the incision rate. Green area indicated 1 sigma solution space.

Figure 11. **(a-d)** The most common types of lateral offset configurations on the sinistral fault (modified from Huang, 1993). The offset scenario of Tohma River according to **(e)** modern channel boundaries on both sides of the fault and (f) between the northern modern channel margin at locations west of the fault and northern margin of the T2 terrace, which is considered to present the oldest channel at locations east of the fault.

TABLE CAPTIONS

Table 1. Sample information for the T1 and T2 terraces of the Tohma River, eastern Turkey.

Table 2. ^{10}Be and ^{26}Al results for samples from the Tohma River in eastern Turkey.

Table 3. Isochron burial ages from the Tohma River, eastern Turkey.

Table 4. Cosmogenic ^{36}Cl data of the depth profile samples from the Tohma River terraces.

Table 5. Results for the Monte Carlo simulations of the depth profile samples from T1 aggradational terraces (after Claude et al., 2019).

SUPPLEMENTARY FIGURE CAPTIONS

Figure S1. The tributaries of the Tohma River around the study area. Black lines indicate swath profiles that shown in Fig. S2 and S3.

Figure S2. The swath profiles of **(a)** N1 and **(b)** N2 at north of the Tohma River showing the positions of T1 and T2 terraces, and their staircase nature. See Fig. S1 for swath profile locations.

Figure. S3. The swath profiles of **(a)** S1, **(b)** S2, **(c)** S3, and **(d)** S4 at south of the Tohma River showing the positions of T1 and T2 terraces, and their staircase nature. Note that the elevation of terraces decreases from west to east. See Fig. S1 for swath profile locations.

Figure S4. Spatial distribution of the T1 (light green polygons) and T2 (dark green polygons) terraces. The originality of terrace surfaces in the north has been altered by ongoing agricultural activity and artificial channel constructions.

SUPPLEMENTARY TABLE CAPTIONS

Table S1. Sample weight change of the isochron-burial samples from the Tohma River (eastern Turkey) during the leaching process. Note that the samples to be dissolved for ^{10}Be and ^{26}Al analyses were selected based on their mineralogy and weight during and after the leaching process.

Table S2. Major and trace element data for the depth profile samples from the Tohma River terraces.

Table S3. Input parameters for the ^{36}Cl depth profile modeling of T1 strath and T2 aggradational terraces (after Claude et al., 2019).

Morphologic Unit	Sample Name	Altitude (m a.s.l.)	Latitude, °N (DD.DD)	Longitude, °E (DD.DD)	Sample Thickness (cm)	Sample Depth (cm)
T2 Aggradational Terrace Isochron burial	THM-IS-T4-1 THM-IS-T4-2 THM-IS-T4-3 THM-IS-T4-4 THM-IS-T4-5 THM-IS-T4-6 THM-IS-T4-7	837	38.511021	38.080003		
T-1 Aggradational Terrace Isochron burial	THM-IS-T2-1 THM-IS-T2-2 THM-IS-T2-3 THM-IS-T2-4 THM-IS-T2-5 THM-IS-T2-6 THM-IS-T2-7 THM-IS-T2-8 THM-IS-T2-9 THM-IS-T2-10 THM-IS-T2-11	752	38.519336	38.095885		
T-1 Strath Terrace Isochron burial	THM-IS-PQ-1 THM-IS-PQ-2 THM-IS-PQ-3 THM-IS-PQ-4 THM-IS-PQ-5 THM-IS-PQ-6 THM-IS-PQ-7	751	38.518432	38.100179		
T-1 Aggradational Terrace Depth Profile	THM-DP-T2-1 THM-DP-T2-2 THM-DP-T2-3 THM-DP-T2-3A THM-DP-T2-4	754	38.51904	38.095889	10 10 10 10 10	35 65 95 125 155

Sample Weight (g)	Carrier Weight (mg)	^{10}Be Concentration (10^4 at/g)	Uncertainty (10^4 at/g)	Uncertainty (%)	Total Al (mg)	Total Al (ppm)	^{26}Al Concentration (10^4 at/g)	Uncertainty (10^4 at/g)	Uncertaint (%)
50.0615	0.2046	8.83	0.4	4.49	17.23	167	60.83	2.48	4.07
47.1644	0.1991	21.66	0.83	3.85	5.83	70	104.41	7.22	6.92
12.0944	0.1989	7.96	0.74	9.27	4.62	85	54.33	3.81	7.02
50.0094	0.198	7.36	0.31	4.26	1.09	12	145.2	8.18	5.63
50.0176	0.1984	29.14	0.95	3.26	9.75	96	227.68	16.12	7.08
50.2454	0.1975	34.07	1.14	3.34	0.79	7	215.92	7.07	3.27
49.999	0.1963	13.36	0.59	4.44	17.86	192	131.06	18.66	14.24
49.9927	0.2043	91.64	2.09	2.28	3.81	77	229.46	6.92	3.02
50.2593	0.1986	24.26	1	4.13	20.03	197	212.96	22.45	10.54
50.0127	0.1977	6.65	0.31	4.73	1.42	14	70.75	7.11	10.05
37.7211	0.1982	5.31	0.39	7.32	7.26	72	90.21	14.64	16.23
50.3911	0.1982	20.78	0.79	3.79	18.5	177	81.36	5.08	6.24
31.3305	0.1986	6.15	0.37	5.94	0.45	9	77.21	6.55	8.48

pectrometry (AMS) measurement errors are at 1σ level, including statistical (counting) error and error due to normalization of standards and blanks. T
ull-process blank ratio is (2.51 ± 0.13) X 10^{-15}. ^{26}Al/^{10}Be ratios are calculated with the CRONUS-Earth exposure age calculator and are referenced to
n.edu/math/ (v. 2.3); Balco et al. (2008) and update from v. 2.2 to v. 2.3 published by Balco in June 2016).

Morphologic Unit	Sample Name	Isochron Slope	Isochron Intercept	Isochron burial age
T2 Aggradational Terrace Isochron burial	THM-IS-T4-1 *THM-IS-T4-2 *THM-IS-T4-3 *THM-IS-T4-4 THM-IS-T4-5 THM-IS-T4-6 **THM-IS-T4-7	3.56 ± 0.23	292000 ± 24800	1.4 ± 0.1 Ma
T-1 Aggradational Terrace Isochron burial	*THM-IS-T2-1 THM-IS-T2-2 THM-IS-T2-3 *THM-IS-T2-4 *THM-IS-T2-5 THM-IS-T2-6 THM-IS-T2-7 THM-IS-T2-8 THM-IS-T2-9 **THM-IS-T2-10 *THM-IS-T2-11	5.26 ± 0.23	613000 ± 53900	540 ± 90 ka
T-1 Strath Terrace Isochron burial	THM-IS-PQ-1 **THM-IS-PQ-2 **THM-IS-PQ-3 *THM-IS-PQ-4 THM-IS-PQ-5 THM-IS-PQ-6 **THM-IS-PQ-7	n.a.	n.a.	n.a.

* used in the isochron-burial age simulation
** statistical outlier, beyond the 2σ solution space
n.a.: not available

Sample Name	Sample Depth (cm)	Sample Dissolved (g)	^{35}Cl spike (mg)	Total Cl (ppm)	^{36}Cl (10^4 at/g)
THM-DP-T2-1	35	50.9635	2.5637	61.1 ± 1.0	240.97 ± 9.47
THM-DP-T2-2	65	55.5205	2.5631	74.8 ± 0.5	230.87 ± 5.35
THM-DP-T2-3	95	66.3842	2.5594	66.5 ± 0.5	165.11 ± 4.17
THM-DP-T2-3A	125	46.3219	2.5558	65.0 ± 0.5	132.03 ± 3.71
THM-DP-T2-4	155	70.4250	2.5576	202.1 ± 0.8	149.08 ± 5.67

AMS measurement errors are at 1 σ level, including the statistical (counting) error and the error due to normalization of standards and blanks.

	T1		
	Age (ka)	**Erosion rate (cm.ka^{-1})**	**Inheritance (x 10^4 at.g^{-1})**
Minimum value	200	0.15	0
Maximum value	1090	0.64	391
Mean value	430	0.36	80
Median value	420	0.36	80
Lowest χ^2 value	300	0.34	2
Mode value	**400**	**0.34**	**79**

Note that reported solution space is within 4σ and erosion rate statistics cannot be used for reporting a value for erosion rate (Hidy et al., 2010).

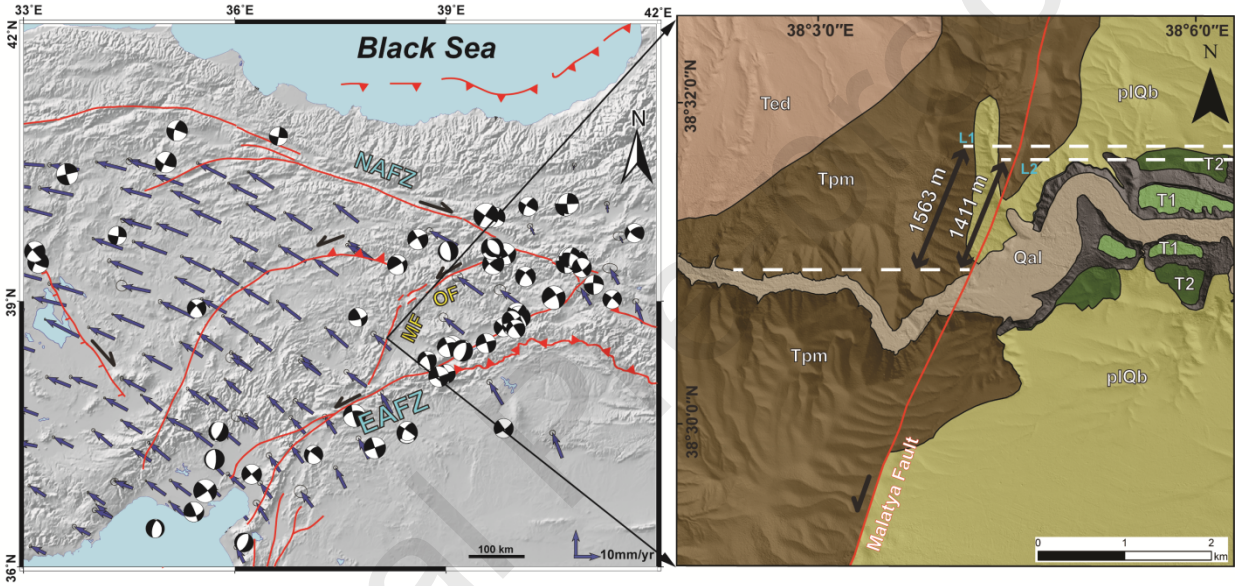

HIGHLIGHTS

The Malatya Fault has a slip rate of 1.0 - 1.12 ± 0.01 mm/yr

The mean uplift rate of the Malatya Fault is 96 ± 11 m/Ma

Our results contradict the claim that the MOFZ is not an active deformation belt

Evolution of the second-order faults of Anatolia supports the tectonic escape model